



## Photosynthetic electron, carbon and oxygen fluxes within a mosaic of Fe limitation in the California Current Upwelling System

5 Yayla Sezginer<sup>1</sup>, Kate Schuler<sup>1</sup>, Emily Speciale<sup>2</sup>, Adrian Marchetti<sup>2</sup>, Claire Till<sup>3</sup>, Ralph Till<sup>3</sup>, Philippe Tortell<sup>1,4</sup>

<sup>1</sup>Department of Earth Oceans and Atmospheric Sciences, University of British Columbia, Vancouver, BC, Canada

<sup>2</sup>Earth Marine and Environmental Sciences, University of North Carolina at Chapel Hill, Chapel Hill, NC, USA

<sup>3</sup>Department of Chemistry, California State Polytechnic University, Humboldt, Arcata, CA, USA

10 <sup>4</sup>Department of Botany, University of British Columbia, Vancouver, BC, Canada

*Correspondence to:* Yayla Sezginer (ysezginer@eoas.ubc.ca)

**Abstract.** We compare primary productivity estimates based on different photosynthetic ‘currencies’ (electrons, O<sub>2</sub> and carbon) collected from the dynamic coastal upwelling waters of the California Current. Fast Repetition Rate Fluorometry and O<sub>2</sub>/N<sub>2</sub>’ measurements were used to collect high-resolution underway estimates of photosynthetic electron transport rates and net community productivity, respectively, alongside on-station <sup>14</sup>C uptake experiments to measure gross carbon fixation rates. Our survey captured two upwelling filaments at Cape Blanco and Cape Mendocino with distinct biogeochemical signatures and iron availabilities, enabling us to examine photosynthetic processes along a natural iron gradient. Significant differences in photo-physiology, cell sizes, Si:NO<sub>3</sub><sup>-</sup> draw-down ratios, and molecular markers of Fe-stress indicated that phytoplankton assemblages near Cape Mendocino were Fe-stressed, while those near Cape Blanco were Fe-replete. Upwelling of O<sub>2</sub>-poor deep water to the surface complicated O<sub>2</sub>-based net community productivity estimates, but we were able to correct for these vertical mixing effects using continuous [N<sub>2</sub>O] surface measurements and depth-profiles of  $\frac{\partial[O_2]}{\partial[N_2O]}$ . Vertical mixing corrections were strongly correlated to sea surface temperature, which serves as an N<sub>2</sub>O-independent proxy for upwelling. Following vertical mixing corrections, all three productivity estimates reflected trends in Fe-stress physiology, indicating greater productivity near Cape Blanco compared to Cape Mendocino. For all assemblages, carbon fixation varied as a hyperbolic function of electron transport rates, but the derived parameters of this relationship were highly variable and significantly correlated with physiological indicators of Fe-stress ( $\sigma_{PSII}$ , Fv/F<sub>M</sub>, Si:NO<sub>3</sub><sup>-</sup> and diatom-specific PSI gene expression), suggesting that iron availability influenced the coupling between photosynthetic electron transport and subsequent carbon fixation. Net community productivity showed strong coherence with daily-integrated photosynthetic electron transport rates across the entire cruise track, with no apparent relationship with Fe-stress. This result suggests that fluorescence-based estimates of gross photochemistry are still a good indicator for bulk primary productivity, even if Fe-limitation influences the stoichiometric relationship between productivity currencies.



## 1 Introduction

35 Along the eastern boundaries of ocean basins, coastal upwelling delivers nutrient-rich deep water to the euphotic zone (Bograd  
*et al.*, 2023), sustaining high phytoplankton growth rates and primary productivity. Despite representing less than 1% of the  
surface ocean, these productive upwelling ecosystems, support ~20% of global fishery catches (Pauly and Christensen, 1995),  
and play a disproportionate role in ocean carbon uptake through the ‘biological carbon pump’ (Mathis *et al.*, 2024). Quantifying  
rates of primary productivity (PP) within eastern boundary currents is thus vital for accurate carbon budgeting and fishery  
yield predictions (Marshak and Link, 2021), yet this remains challenging due to the highly dynamic nature of these systems.

40 The California Current system (CCS) is one of the best studied eastern boundary currents, extending from British Columbia,  
Canada, to Baja California, Mexico. Upwelling in the CCS occurs during spring and summer when northerly winds drive  
Ekman transport of surface water offshore. Within the upwelling season, short-term changes in windspeed and direction can  
dampen or reverse upwelling signals on the scale of hours to days, while complex coastline geometry directs wind flow,  
45 creating upwelling hotspots in the lee of capes (Castelao and Luo, 2018). Underlying bathymetric features and deep-water  
composition further influence the nature of upwelling filaments and the availability of macro and micro nutrients. In regions  
with shallow and wide continental shelves, sediment deposition provides a primary source Fe and other micronutrients  
(Deutsch *et al.*, 2021). In contrast, waters overlying steep narrow shelves retain less Fe, and PP in these regions can be limited  
by Fe availability despite the presence of upwelling conditions (Biller *et al.*, 2013). The resulting ‘mosaic of Fe limitation’  
50 influences the distribution of phytoplankton biomass and productivity across the CCS (Hutchins *et al.*, 1998; Till *et al.*, 2019).  
Resolving ecosystem responses to such a heterogenous environment requires high resolution measurements.

Traditionally, primary productivity has been measured using discrete bottle incubations where the net change in dissolved O<sub>2</sub>  
or particulate organic carbon is measured over time. Shorter incubations approximate gross primary productivity (GPP),  
55 whereas longer incubations allow time for respiration to act upon tracers, yielding estimates somewhere between GPP and net  
PP (NPP = GPP – respiration). Although bottle incubations are still widely used to directly observe carbon fixation rates, the  
resulting measurements can be ambiguous in terms of GPP vs. NPP, while also providing low sampling resolution and posing  
potential containment artefacts (Banse, 2002). To avoid these challenges, a number of high through-put PP proxies have been  
developed based on advances in dissolved gas measurements, bio-optical techniques, and satellite-based ocean color  
60 observations (Balch *et al.*, 2021). These diverse PP methodologies target different photosynthetic processes, from subcellular  
light absorption to ecosystem scale carbon export.

At the smallest spatial and temporal scales, Photosystem II (PSII) electron transport rates (ETR<sub>PSII</sub>) quantify light absorption  
and conversion to chemical energy for a variety of metabolic activities including carbon fixation. Measurements of ETR<sub>PSII</sub>  
65 can be obtained from active chlorophyll fluorescence techniques, which exploit the inverse relationship between PSII  
fluorescence and photochemical yields to enable non-invasive and high-frequency measurement from underway seawater lines  
(Kranz *et al.*, 2020; Sezginer *et al.*, 2023) or autonomous platforms (e.g. Carvalho *et al.*, 2020). Downstream of ETR<sub>PSII</sub>, carbon  
fixation can be directly measured using bottle incubations, or approximated from empirical algorithms relating NPP to  
remotely sensed Chlorophyll (Chl) concentration, sea surface temperature (SST), and photosynthetically available radiance  
70 (PAR) (Behrenfeld and Falkowski, 1997; Behrenfeld *et al.*, 2005; Saba *et al.*, 2011). Finally, net community productivity  
(NCP), represents the difference between GPP and community respiration and can be equated to carbon export out of the  
mixed layer. This term can be derived from measurements of biological oxygen saturation, ΔO<sub>2</sub>/Ar, using Ar-normalization of  
O<sub>2</sub> to correct for physical influences on gas disequilibria (e.g. temperature or salinity changes or bubble injection) to isolate  
the biological signal (Craig and Hayward, 1987; Cassar *et al.*, 2009). Assuming steady-state conditions, O<sub>2</sub> fluxes from the  
75 mixed layer represent a balance between net biological production and sea-air exchange, allowing the calculation of NCP from  
sea-air flux estimates. Steady state assumptions are violated in upwelling systems, such as the CCS, where O<sub>2</sub> fluxes in the  
mixed layer are also affected by vertical mixing. However, such vertical mixing effects can be corrected using N<sub>2</sub>O as a tracer

of O<sub>2</sub>-depleted deep water, as oxygen-consuming N<sub>2</sub>O production pathways are photo-inhibited at the surface, resulting in fixed subsurface N<sub>2</sub>O to O<sub>2</sub> ratios in the ocean (Cassar, Nevison and Manizza, 2014).

80

The various measurement techniques described above yield PP estimates in a number of different ‘currencies’, i.e. carbon, oxygen and electrons, each with different integration time scales (seconds to weeks). In theory, combining PP quantification approaches can fill data gaps (e.g. cloud or ice interference with satellite data, or missing years in time series operations), and provide deeper understanding of ocean metabolism. In practice, incorporating alternative measurement approaches requires understanding of conversion rates between the various PP currencies. Predicting these conversion factors is challenging, as they vary in response to environmental conditions and phytoplankton taxonomy and physiology (Halsey and Jones, 2015; Schuback *et al.*, 2017; Hughes, Varkey, *et al.*, 2018; Hughes *et al.*, 2021). For example, the ETR<sub>PSII</sub> : GPP ratio often exceeds the theoretical stoichiometry of 4 (Halsey and Jones, 2015), implying that redox potential generated at PSII is used for functions other than carbon fixation, such as nitrogen uptake or cyclic electron transport. Similarly, differences between ETR<sub>PSII</sub> and NCP represent combined O<sub>2</sub> consumption pathways, including cellular respiration, chloro- and photorespiration and pseudo cyclic electron transport. Investigating the drivers of decoupling between currencies can thus improve conversion rate estimates, and also provide insights into energy transfer efficiencies between different components of the photosynthetic process.

85

90

95

100

Here we present simultaneous PP measurements in the CCS collected using high resolution, underway sampling techniques along a cruise track between Newport, OR and San Francisco, CA. Underway measurements of ETR<sub>PSII</sub> and NCP were conducted during the May-June upwelling season of 2023 and were complemented with parallel measurements of ETR<sub>PSII</sub> and <sup>14</sup>C-GPP collected at oceanographic stations. Our results demonstrate fine-scale spatial patterns in GPP and NCP associated with variability in localized upwelling filaments, with particularly notable differences observed across gradients of dissolved iron concentrations resulting from varying coastal bathymetry. These results enable us to examine variability in productivity currency conversion factors across natural Fe availability gradients within the California Current System, with potential application to other complex coastal waters.

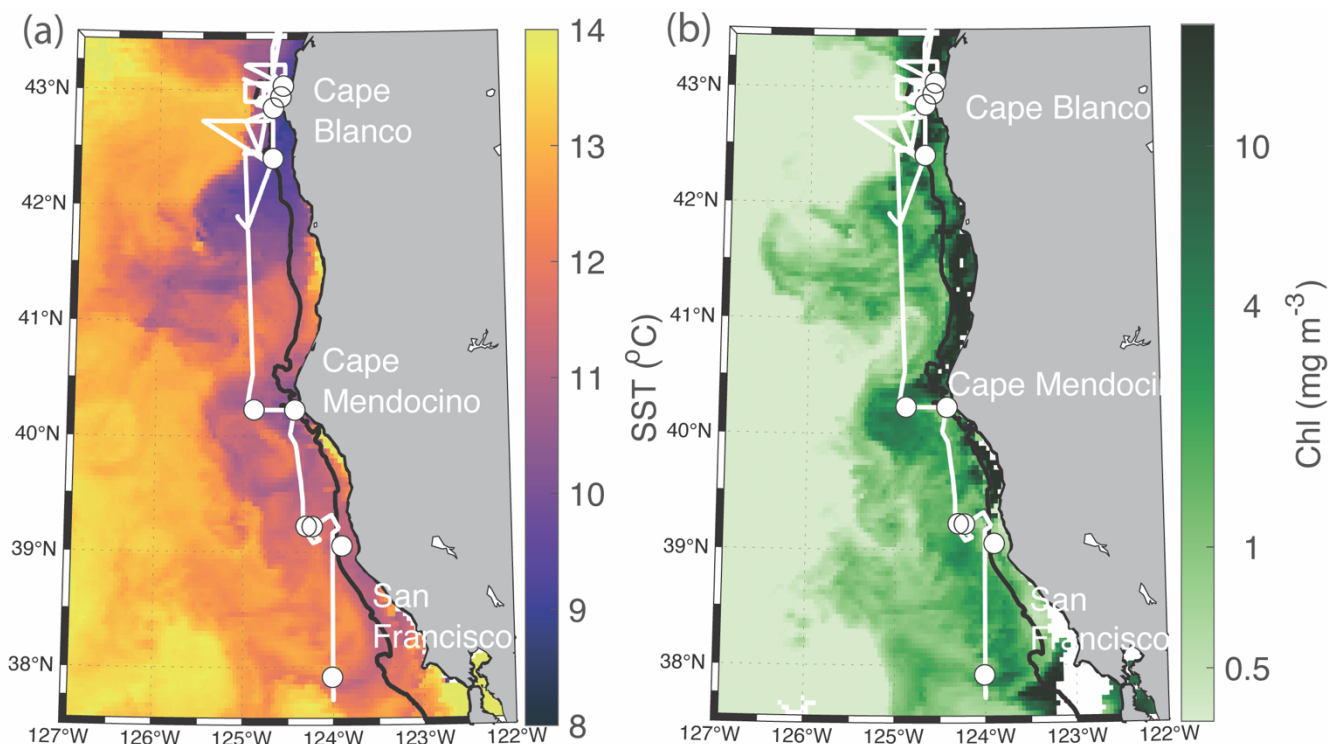
## 2 Methods and Materials

### 2.1 Sampling Sites

105

Measurements were collected along the Oregon and Northern California coast during the Phytoplankton UPwelling Cycle (PUPCYCLE II) expedition, onboard the *R/V Sally Ride* from May 27 – June 11, 2023. A key objective of the program was to examine the evolution of phytoplankton blooms in recently upwelled waters, and we specifically targeted two upwelling plumes off Cape Blanco and Cape Mendocino, which were identified by low sea surface temperature (SST < 10°C; Figure 1). Along the cruise track, temperature, salinity, and chlorophyll fluorescence were monitored by the ship’s underway system, supplied by a seawater supply line with a nominal intake depth of approximately 5m. Nitrate concentrations were measured continuously with a Seabird SUNA sensor. In addition to standard oceanographic variables, the seawater supply line was also used for continuous underway measurements of phytoplankton photo-physiology and ETR<sub>PSII</sub> using a Fast Repetition Rate fluorometer (FRRF; Soliense Inc.), and NCP using a custom-built Pressure In-Situ Gas Instrument (PIGI), as described below.

110



115

**Figure 1. Study site map.** Location of the cruise track (white line) and discrete sampling stations (white circles) during the PUPCYCLE expedition. The black bathymetric contour line represents the 200 m isobath. The study region and surrounding waters are colored by **a.** daily NASA Aqua Modis Level 3 satellite retrievals of Chl concentration (Chl) averaged over the cruise period (May 27 – June 11, 2024) **b.** NASA Aqua Modis Level 3 satellite retrievals of Sea Surface Temperature (SST) averaged over the cruise period.

120

Daily CTD and rosette casts were conducted one hour before local sunrise, and samples were collected at four depths targeting 1%, 10%, 22%, and 46% of surface solar irradiance levels. Photosynthesis-Irradiance (PI) curves (measured with Fast Repetition Rate fluorometry– see below), chlorophyll *a* (Chl) and nutrient concentrations ( $\text{NO}_3^-$ , Si,  $\text{PO}_4$ , Fe) were measured at all four depths. Samples collected from 1% and 46% irradiance levels were also incubated for  $^{14}\text{C}$ -based PI curves (see sect. 2.5), with sub-samples collected for High Performance Liquid Chromatography (HPLC)-based analysis of phytoplankton pigments.

125

## 2.2 Fast Repetition Rate Fluorometry

A bench-top Soliense Inc. Fast Repetition Rate Fluorometer (FRRF) was configured for underway collection of chlorophyll *a* fluorescence transients following Sezginer *et al.*, (2021). Samples were introduced to the measurement cuvette by an integrated peristaltic pump. The pump was used to flush the measurement cuvette for 2.5 minutes before isolating a sample for analysis. Following a one-minute dark period to relax short lived non-photochemical quenching, five single-turnover fluorescence transients were collected from each sample in the dark. Each single-turnover transient included a sequence of 100 sub-saturating excitation light pulses of  $1.5 \mu\text{s}$  duration, and a  $1 \mu\text{s}$  interval between pulses. The excitation phase is designed to stimulate photochemistry and gradually reduce the pool of primary electron acceptor molecules,  $Q_a$  (Kolber, Prášil and Falkowski, 1998). As the  $Q_a$  pool is reduced, further electron exchange between PSII and  $Q_a$  is prevented, closing the photochemistry pathway and causing a concurrent increase in PSII fluorescence yields. The excitation phase is followed by a relaxation sequence consisting of 127 light pulses with an initial  $20 \mu\text{s}$  interval. During the relaxation phase, the interval

135

130



140 between light pulses increases exponentially, enabling  $Q_a$  reoxidation between pulses to gradually reopen the photochemistry pathway, such that fluorescence yields return to their basal levels. The biophysical model described by Kolber, Prášil and Falkowski (1998) was fit to the resulting fluorescence transient to derive the maximum quantum yield of PSII ( $F_v/F_m$ ), functional absorption area of PSII ( $\sigma_{PSII}$ ), and turnover rate of the primary electron acceptor  $Q_a$  ( $\tau_{Qa}$ ).

### 2.3 Electron Transport Rates, $ETR_{PSII}$

145 Continuous FRRF sampling was interrupted every 12 samples (~3hrs) to conduct a Photosynthesis-Irradiance (PI) curve characterizing light-dependent changes in photo-physiology and photochemistry. Across the entire cruise, we collected 91 PI curves. Each PI curve was initiated with a fresh sample, and consisted of 11 light levels, increasing from 0 – 850  $\mu\text{mol photons m}^{-2} \text{s}^{-1}$ . Light was supplied evenly by the five actinic LEDs within the FRRF (445, 470, 505, 530, and 590 nm). At each light level,  $ETR_{PSII}$  was calculated following Suggett and Moore (2010):

$$ETR_{PSII} = PAR * \sigma'_{PSII} * \frac{F'_q}{F'_v} * 6.033 * 10^{-3} \quad 1.$$

150 In this formulation, the rate of photon delivery to the pool of PSII reaction centers (RCII) is derived as the product of photosynthetically active radiation (PAR; units  $\mu\text{mol photons m}^{-2} \text{s}^{-1}$ ) supplied by the LED lamps, and the wavelength-specific functional absorption area of RCII ( $\sigma'_{PSII}$ ; units of  $\text{\AA}^2 \text{PSII}^{-1}$ ). The conversion efficiency from light to photochemical energy depends on the fraction of open RCII, measured as the dimensionless ratio between the fluorescence amplitude measured under actinic light when photochemistry is active ( $F'_q = F'_m - F'$ ) and that measured under actinic light if all RCII were oxidized, ( $F'_v = F'_m - F'_o$ ). In practice, measuring the minimum fluorescence when the RCII pool is completely open ( $F'_o$ ) is challenging, as actinic light always drives some degree of photochemistry and reduction of RCII. Alternatively,  $F'_o$  can be derived as  $F_o/(F_v/F_m + F_o/F'_m)$ , following Oxborough *et al.*, (2012).

160 The prime notation (') refers to FRRF parameters derived under actinic light. The constant  $6.033 * 10^{-3}$  converts PAR to units of quanta  $\text{m}^{-2} \text{s}^{-1}$ , and  $\sigma'_{PSII}$  to units of  $\text{m}^2 \text{RCII}^{-1}$ , so the final units of  $ETR_{PSII}$  are quanta  $\text{s}^{-1} \text{RCII}^{-1}$ . For a complete description of FRRF derived parameters, see Schuback *et al.* (2021) and (Tortell, Schuback and Suggett, 2023).

165 For each light curve measured,  $ETR_{PSII}$  was plotted against PAR and fit with the photosynthesis-irradiance model of Platt *et al.* (Platt, Gallegos and Harrison, 1980):

$$ETR_{PSII} = P_s \left( 1 - e^{-\frac{\alpha PAR}{P_s}} \right) e^{-\frac{\beta PAR}{P_s}} \quad 2.$$

170 During the initial light-limiting part of the curve,  $ETR_{PSII}$  increases linearly with PAR with a slope of  $\alpha$ . As PAR increases to saturating levels,  $ETR_{PSII}$  stabilizes at maximum levels,  $P_{max}$ . The light saturation index,  $E_k$  is derived as  $P_{max}/\alpha$ . When phytoplankton are affected by photoinhibition,  $\beta$  describes the decrease in  $ETR_{PSII}$  at high light levels (i.e.  $\gg E_k$ ). In the absence of photoinhibition,  $P_s = P_{max}$ . When photo-inhibition is present ( $\beta > 0$ ),  $P_s$  represents the theoretical maximum potential  $ETR_{PSII}$ . When  $\beta > 0$ ,  $P_{max}$  is derived as:

$$P_{max} = P_s \left( \frac{\alpha}{\alpha + \beta} \right) \left( \frac{\beta}{\alpha + \beta} \right)^{\left( \frac{\beta}{\alpha} \right)} \quad 3.$$

175 To evaluate  $ETR_{PSII}$  over the cruise track, we linearly interpolated derived values of  $\alpha$ ,  $\beta$ , and  $P_s$  to the sampling resolution of continuous PAR measurements from the ship's meteorological tower (Biospherical Inst. QSR-240P). In-situ mean mixed layer PAR was estimated by accounting for light attenuation with depth, quantified by the diffuse attenuation coefficient ( $K_d = \ln(\text{PAR}_0/\text{PAR}_{\text{mld}})/(\text{mld} - 0)$ ), where  $\text{PAR}_0$  is PAR measured at the surface and  $\text{PAR}_{\text{mld}}$  is PAR measured at the mixed layer





180 depth (mld) (Domingues and Barbosa, 2023). For each CTD cast ( $n = 28$ ), mld was determined using a density difference criterion of  $0.125 \text{ kg m}^{-3}$ , and  $\text{PAR}_{\text{mld}}$  was measured with a Biospherical QSP-200 PAR sensor mounted to the CTD rosette. Both  $K_d$  and mld were linearly interpolated to the resolution of continuous PAR measurements. Finally, in-situ PAR was estimated as,

$$\text{PAR}_{\text{in situ}} = \text{PAR}(1 - e^{-K_d \text{MLD}})(K_d * \text{mld})^{-1} \quad 4.$$

185 To compare  $\text{ETR}_{\text{PSII}}$  with NCP (Sect. 2.6), we converted  $\text{ETR}_{\text{PSII}}$  from  $\text{e}^- \text{RCII}^{-1} \text{ s}^{-1}$  to volumetric units of  $\text{mmol O}_2 \text{ m}^{-2} \text{ d}^{-1}$ . This conversion requires an estimate of the chlorophyll content of RCII, which is known to vary significantly across phytoplankton in response to taxonomic and environmental influences (Greene *et al.*, 1992; Murphy *et al.*, 2017; Aardema *et al.*, 2024). Following previous authors (Kolber and Falkowski, 1993; Schuback, Schallenberg, Duckham and Maldonado, 2015), we assumed a possible range of Chl to RCII ratios of 400 to 700, yielding upper and lower bounds of Chl-normalized  $\text{ETR}_{\text{PSII}}$ .

$$\text{GP} = \text{ETR}_{\text{PSII}} * 86400 * (\text{Chl:RCII})^{-1} * \text{Chl} * \text{mld} * \frac{1}{4} \quad 5.$$

190 To obtain volumetric units, Chl-normalized ETR was multiplied by mixed layer Chl concentrations ( $\text{mmol Chl m}^{-3} * \text{mld}$ ), assuming homogenous [Chl] throughout the mixed layer. Multiplying by 86400 converts from  $\text{s}^{-1}$  to  $\text{d}^{-1}$ . Given that four charge separation events are required per  $\text{O}_2$  evolved, ETR was divided by 4 for final gross photochemistry (GP) estimates in terms of  $\text{mmol O}_2 \text{ m}^{-2} \text{ d}^{-1}$ .

## 2.4 Non-Photochemical Quenching, NPQ

195 Under excess irradiance, light supply to PSII outpaces maximum downstream electron transport rates, creating the potential for dangerous reactive oxygen species (ROS) to accumulate (Müller, Li and Niyogi, 2001). To mitigate excess excitation, photoautotrophs have evolved a number of photoprotective mechanisms, including non-photochemical quenching (NPQ), which dissipates excitation absorbed by PSII as heat, thereby reducing PSII photochemical and fluorescence yields. Previously, NPQ has been quantified from FRRF data as Stern-Volmer quenching, defined as the relative decrease in PSII fluorescence in response to light exposure:  $\text{NPQ}_{\text{SV}} = (F_m - F'_m)/F'_m$ . However, this formulation does not account for longer-lived NPQ mechanisms that may still be active during dark measurements following recent high light exposure. To overcome this limitation, we used the normalized Stern-Volmer parameter ( $\text{NPQ}_{\text{NSV}}$ ), calculated as  $F'_o/F'_v$  (McKew *et al.*, 2013). For each PI curve measured,  $\text{NPQ}_{\text{NSV}}$  was plotted against PAR and fit with a single component exponential curve. In-situ  $\text{NPQ}_{\text{NSV}}$  was then estimated by interpolating the resulting curve fits to in-situ PAR values.

## 205 2.5 $^{14}\text{C}$ -uptake experiments

During daily station sampling, 200 mL were collected from 1% and 46% light level depths (approximately 50 and 10 meters, respectively) into acid washed 250 mL bottles for  $^{14}\text{C}$  incubations. Samples were immediately spiked with  $150 \mu\text{Ci}$  of  $\text{H}^{14}\text{CO}_3$  (Perkin Elmer), and inverted to homogenize the contents of the bottles. The homogenized media was then aliquoted into 20 mL borosilicate scintillation vials, which were incubated over 3 hours in a custom-built photosynthesetron at 7 light levels from 0 –  $650 \mu\text{mol photons m}^{-2} \text{ s}^{-1}$ . At the end of the incubation, the entire content of the vials was filtered onto 25mm GF/F filters with a nominal pore size of  $0.7 \mu\text{m}$ . Filters were fumed with 10% HCl for 24 hours to remove any inorganic carbon prior measuring activity on filters with an on-board scintillation counter (Beckman LS 6500). Immediately after spiking samples, three vials were filtered for triplicate time zero measurements. Three  $100 \mu\text{L}$  aliquots were also taken from the initial 200 mL sample and treated with  $100 \mu\text{L}$  of 3M NaOH to measure total  $^{14}\text{C}$  counts. Disintegrations per minute were converted into hourly C fixation rates according to Knapp *et al.*, (1996).



## 2.6 Net Community Productivity (NCP)

We measured NCP based on mixed layer concentrations of O<sub>2</sub> and N<sub>2</sub> obtained from the Pressure of In-Situ Gas Instrument (PIGI), following Izett and Tortell, 2021 and Izett *et al.*, 2021. This method estimates NCP from the biological oxygen saturation anomaly, ΔO<sub>2</sub>/N<sub>2</sub><sup>'</sup>, using N<sub>2</sub><sup>'</sup> as an analog for Argon (Ar) to correct for physical effects on O<sub>2</sub> saturation. In this method, net community productivity is equated to the sea-air flux of O<sub>2</sub> as determined by the biological saturation anomaly (ΔO<sub>2</sub>/N<sub>2</sub><sup>'</sup>) scaled by the [O<sub>2</sub>] in equilibrium with the atmosphere ([O<sub>2</sub>]<sub>sat</sub>), and the O<sub>2</sub> piston velocity (*k*<sub>O<sub>2</sub></sub>).

$$\text{NCP} = k_{O_2} * \frac{\Delta O_2}{N_2'} * [O_2]_{\text{sat}} \quad 6.$$

The PIGI enables cost effective measurements of ΔO<sub>2</sub>/N<sub>2</sub><sup>'</sup> using an oxygen optode and a gas tension device rather than a mass spectrometer, which is more commonly used to measure ΔO<sub>2</sub>/Ar (Izett and Tortell, 2020). In this method, N<sub>2</sub><sup>'</sup> is derived as an approximation of Ar, using model calculations that quantify differences between Ar and N<sub>2</sub> concentrations due primarily to solubility changes and bubble processes. A full description of the 1D model applied to estimate N<sub>2</sub><sup>'</sup> is available in Izett and Tortell (2021). The model uses ancillary data, including windspeed, mixed layer depth, temperature, salinity, and sea level pressure, to estimate changes in mixed layer Ar and N<sub>2</sub> concentrations over one residence time period prior to sampling. We applied a residence time of 14 days for this region where mixed layer gas residence times are strongly influenced by the timescales of upwelling events (Austin and Barth, 2002). Ancillary datasets required for N<sub>2</sub><sup>'</sup> calculations were obtained from a combination of satellite observations and model products, and are compiled in the Supplement S1, alongside descriptions of each data source. The 1D model calculations and code are available at [https://github.com/rizett/O2N2\\_NCP\\_toolbox](https://github.com/rizett/O2N2_NCP_toolbox) with example calculations.

Additional corrections to NCP estimates were made to account for vertical mixing fluxes, which transport low O<sub>2</sub> water to the surface (Izett *et al.*, 2018). Previous studies have omitted ΔO<sub>2</sub>/Ar data collected in known upwelling areas, where the assumption of limited vertical mixing fluxes on ΔO<sub>2</sub>/Ar variability is violated (e.g. Stanley *et al.*, 2010). To address this limitation, Cassar, Nevison and Manizza (2014) developed an approach to use surface measurements of N<sub>2</sub>O to quantify vertical transport of low O<sub>2</sub> waters. In marine environments, there is a strong stoichiometric relationship between apparent oxygen utilization and N<sub>2</sub>O, which is produced as a by-product of subsurface oxygen-consuming N remineralization pathways (Elkins *et al.*, 1978). These N<sub>2</sub>O production pathways are thought to be photo-inhibited within the euphotic zone (Horrigan, Carlucci and Williams, 1981; Olson, 1981), so that excess N<sub>2</sub>O concentrations in the mixed layer serve as a tracer for vertical influxes of O<sub>2</sub>-depleted subsurface water. We note that several recent studies have observed nitrification within the euphotic zone, challenging the assumption that N<sub>2</sub>O production is limited to subsurface waters (Grundle, Juniper and Giesbrecht, 2013; Smith *et al.*, 2014). However, a sensitivity analysis by Izett *et al.* (2018) determined the potential effects of euphotic zone nitrification introduced a nearly negligible error to NCP estimates in regions with high productivity and high mixing rates, as is the case in the CCS. We thus used the approach of Cassar, Nevison and Manizza (2014) and Izett *et al.*, (2018), to correct for vertical mixing following Eq. 7.

$$\text{NCP} = k_{O_2} * \left( \frac{\Delta O_2}{Ar} * [O_2]_{\text{sat}} - \frac{k_{N_2O}}{k_{O_2}} * \frac{\partial [O_2]^B}{\partial [N_2O]^B} * [N_2O]^B \right) \quad 7.$$

This mixing correction uses surface measurements of N<sub>2</sub>O super-saturation ([N<sub>2</sub>O]<sup>B</sup>), the ‘supply ratio’ of oxygen saturation, given by the vertical gradient of biological O<sub>2</sub> to N<sub>2</sub>O ( $\frac{\partial [O_2]^B}{\partial [N_2O]^B}$ ), and the ratio of gas transfer velocities ( $\frac{k_{N_2O}}{k_{O_2}}$ ). The surface water saturation of N<sub>2</sub>O, [N<sub>2</sub>O]<sup>B</sup>, was derived based on the difference between the N<sub>2</sub>O saturation anomaly and changes in N<sub>2</sub>O solubility due to recent heat fluxes ([N<sub>2</sub>O]<sub>meas</sub> - [N<sub>2</sub>O]<sub>sat</sub> - [N<sub>2</sub>O]<sub>thermal</sub>). Heat flux effects on solubility, [N<sub>2</sub>O]<sub>thermal</sub>, were derived following Keeling and Shertz (1992), with corrections from Jin *et al.* (2017). Surface [N<sub>2</sub>O]<sub>meas</sub> was continuously measured from the surface seawater supply with an integrated cavity output spectroscopy (OA-ICOS) gas analyzer (Los Gatos Research, N<sub>2</sub>O/CH<sub>4</sub> Analyzer, Model Number: 913-0055) coupled to a gas extraction module (Schuler and Tortell, 2023). The region-specific supply ratio,  $\frac{\partial [O_2]^B}{\partial [N_2O]^B}$ , was calculated by taking the slope of subsurface [O<sub>2</sub>]<sup>B</sup> plotted against subsurface [N<sub>2</sub>O]<sup>B</sup>.



260 The compiled data across the cruise track resulted in a supply ratio of  $-1.6 * 10^4 \pm 0.3 * 10^4$  mmol O<sub>2</sub> (mmol N<sub>2</sub>O)<sup>-1</sup>, which is similar to previous measurements for the Northeast Pacific ( $-1.8 * 10^4$ ; Izett et al., 2018) and global basins ( $-1.5 * 10^4$ ; (Cassar, Nevison and Manizza, 2014). Following Cassar, Nevison and Manizza (2014), we assumed a constant  $\frac{K_{N_2O}}{K_{O_2}}$  ratio of 0.92. Total uncertainty was determined by following Izett (2021).

## 2.7 Nutrient concentrations

265 Samples collected during daily productivity casts were analysed for dissolved NO<sub>3</sub><sup>-</sup> + NO<sub>2</sub><sup>-</sup>, PO<sub>4</sub><sup>3-</sup>, and silicic acid concentrations. Thirty mL were collected from niskin bottles and filtered onto GF/F filters, using acid-washed syringes into 20mL HDPE scintillation vials. Samples were kept frozen before analysis on a OI Analytical Flow Solutions IV auto analyzer by Wetland Biogeochemistry Analytical Services at Louisiana State University. Detection limits were 0.09 μmol L<sup>-1</sup> for nitrate + nitrite, 0.02 μmol L<sup>-1</sup> for phosphate and 0.02 μmol L<sup>-1</sup> for silicic acid. Reference standards for dissolved nutrients in seawater were used to ensure quality control.

275 Samples for iron analysis were collected with a rosette of Teflon-coated OTE-bottles during a separate cast directly after the daily sampling cast. After recovery, OTE-bottles were taken directly to a trace metal-clean sampling van where they were pressurized with filtered compressed air. Surface samples (~3 m depth) were also collected with a tow-fish system plumbed into the trace metal van, as in Bruland *et al.* (2005). All samples were passed through pre-cleaned 0.2 micrometer Supor membrane Acropak capsule filters into trace metal cleaned bottles (Cutter *et al.*, 2014). Samples were acidified to pH 1.8 with optima HCl, and analyzed post-cruise with a flow injection analysis method (Lohan, Aguilar-Islas and Bruland, 2006), with modifications as in Biller *et al.* (2013). Briefly, this method involved pre-concentrating the Fe at pH 2 with Toyopearl Chelate-650 resin and eluting into a reaction stream containing the colorimetric agent N,N-dimethyl-p-phenylenediaminedihydrochloride (DPD). The absorbance of the reaction stream was measured with a flow-through spectrophotometer. Calibration was performed with a standard addition curve, and blanks were assessed using acidified MilliQ. Reference samples analysed to assess accuracy compared well to consensus values: SAFe D1 0.70 +/- 0.04 nmol Fe/kg, n=12 compared with consensus value 0.67 +/- 0.04 nmol/kg, and GEOTRACES GSC 1.51 +/- 0.07 nmol/kg (n=11) compared with consensus value 1.53 +/- 0.11 nmol/kg.

## 285 2.8 Transcriptomic analysis

Surface niskins (46% surface irradiance) collected during daily productivity casts were subsampled for RNA extraction. Approximately 2.5L to 4L of seawater were filtered onto 0.8 μm Pall Supor filters (142 mm) using a peristaltic pump, and then flash frozen in liquid nitrogen and stored at -80 °C. RNA was extracted using the RNAqueous-4PCR kit, following manufacturer instructions with the incorporation of a bead beating step during RNA lysis. All RNA samples were sent to GENEWIZ for library preparation and sequencing with PolyA tail selection. Sequencing was performed on an Illumina HiSeq 4000 with a 2x150 bp configuration. GENEWIZ provided raw paired-end read sequences for each sample.

Raw reads were trimmed using Trim Galore 0.6.10 (Martin, 2011) and quality control was determined with FastQC (Andrews, 2010). A *de novo* metatranscriptome assembly was conducted using rnaSPAdes 3.15.5 (Bushmanova *et al.*, 2019) and CD-HIT-EST (Li and Godzik, 2006). Contigs were annotated using the Marine Functional Eukaryotic Reference Taxa (MarFERReT) database (Groussman *et al.*, 2023), which provides NCBI taxonomic annotations (Federhen, 2012) and Pfam 34.0 functional annotations (Mistry *et al.*, 2021). Samples were mapped against the MarFERReT DIAMOND sequencing aligner and its compatible BLASTX command (e-value < 1e-06) (Buchfink, Xie and Huson, 2015). Trimmed samples were aligned using Salmon (Patro *et al.*, 2017). The package tximport (Soneson, Love and Robinson, 2016) was used to generate a comprehensive table of read count data for each sample and each contig. Only counts taxonomically mapping to Bacillariophyta (i.e., diatoms) were included. The normalized counts for all genes were then calculated using DESeq2's median of ratios method (Love, Huber and Anders, 2014). Normalized counts of the low iron-inducible periplasmic protein (Fea1)





(Allen *et al.*, 2007), which shows high similarities to Iron Starvation-Induced Protein 2A (ISIP2A) (Behnke and LaRoche, 2020), was used as an indicator for iron stress (Marchetti *et al.*, 2017).

## 2.7 Pigment Concentrations and Taxonomic Compositions

305 During daily productivity casts, duplicate 1L dark Nalgene bottles were filled with water from niskin bottles collected at 1%  
and 46% PAR level depths. Under low ambient light, samples were filtered onto 47mm GFF filters (Whatman, nominal pore  
size 0.7  $\mu\text{m}$ ). Filters were immediately flash frozen and stored in an onboard  $-80^{\circ}\text{C}$  freezer. Samples were shipped on dry ice  
to the Pinckney Estuarine Ecology Photopigment Analysis Facility at the University of Southern California. There,  
310 photopigment concentrations were determined with high performance liquid chromatography following (Pinckney *et al.*,  
2001). Pigment compositions are reported in Appendix 2.

In addition to pigment sampling, Light microscopy was used to identify and enumerate dominant phytoplankton taxa. For  
microscopic cell counts, 25-50 mL subsamples preserved in Lugol's solution were concentrated by sedimentation using  
Utermöhl chambers for  $>24\text{h}$  (Lund, Kipling and Le Cren, 1958). Cell counts of recognizable dinoflagellate and diatom  
315 genera were carried out using an Olympus CKX-31 inverted microscope in at least ten fields of view per sample at 200x and  
400x magnification.

## 3 Results

### 3.1 Oceanographic conditions

Across the cruise track, sea surface temperature (SST) ranged from 8.5 to 14  $^{\circ}\text{C}$  (Fig. 2), with strong coastal to offshore  
320 gradients (Fig. 1 and 2). The lowest SST were observed within near-shore upwelling plumes, which were associated with high  
salinity ( $> 33$  psu). Along the entire cruise transect, salinity was negatively correlated with SST ( $\rho = -0.73$ ,  $p \ll 0.01$ ), as  
expected for upwelling regions. Sharp hydrographic fronts were apparent along coastal to offshore transects. Moving offshore,  
SST rapidly increased, while salinity dropped, changing by as much as 2 degrees and 0.5 psu, respectively, within a span of 5  
325 km. These results indicate the presence localized on-shore upwelling plumes, as compared to more homogenous off-shore  
waters. Within the upwelling plumes,  $\text{NO}_3^-$  concentrations were elevated, reaching maximum concentrations of 20.5  $\mu\text{M}$  and  
displaying a positive relationship with salinity ( $\rho = 0.89$ ,  $p \ll 0.01$ ) and a negative relationship with SST ( $\rho = -0.76$ ,  $p \ll$   
0.01). Off-shore,  $\text{NO}_3^-$  decreased to concentrations below the SUNA detection limit ( $\sim 0.3 \mu\text{M}$ ), highlighting the difference in  
nutrient availability between the oligotrophic offshore waters and productive coastal upwelling environments. Chlorophyll  
330 concentrations varied between 0.04 to 5.6  $\text{mg m}^{-3}$  and exhibited a statistically significant (though weak) positive relationship  
with  $\text{NO}_3^-$  ( $\rho = 0.30$ ,  $p \ll 0.01$ ).

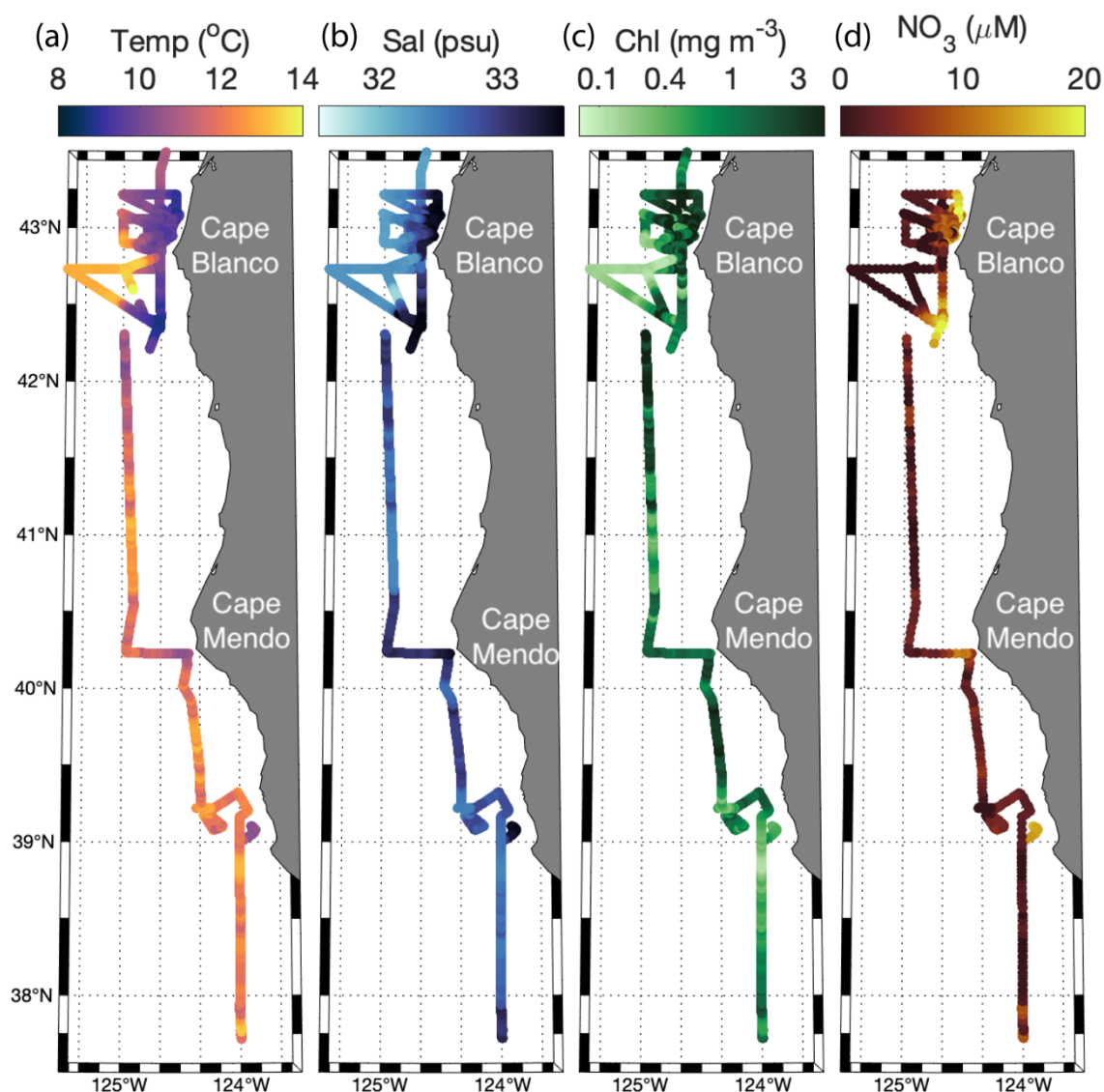


**Figure 2. Surface water (a) SST, (b) salinity, (c) Chl, and (d) NO<sub>3</sub><sup>-</sup> along the cruise track. Cape Mendocino is abbreviated as Cape Mendo.**

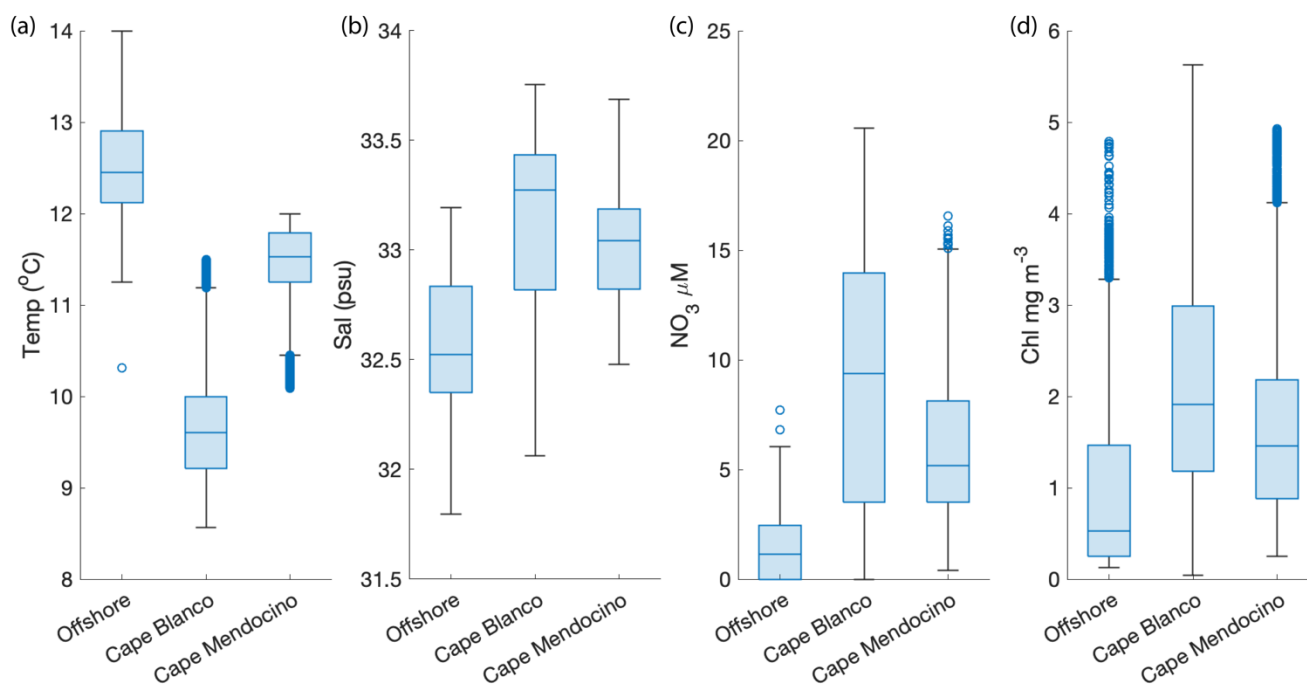
335

In addition to the coastal-offshore gradient, surface water hydrography also differed between the two distinct upwelling plumes we sampled. These plumes were identified as low SST in the lees of Cape Blanco and Cape Mendocino (Fig 1). Both plumes exhibited an upwelling signature, but the apparent intensity of upwelling (as reflected in SST, salinity, NO<sub>3</sub><sup>-</sup>, and Chl) was significantly stronger within the northern Cape Blanco plume (Fig. 3). Most apparently, SST was several degrees cooler at Cape Blanco (median of  $9.6 \pm 0.4$  °C) than at Cape Mendocino (median of  $11.5 \pm 0.01$  °C). Nitrate concentrations were highly variable across both plumes, but the mean NO<sub>3</sub><sup>-</sup> at Cape Blanco ( $9.4 \pm 0.8$  μM) was nearly twice as high as that of Cape Mendocino ( $5.2 \pm 0.4$  μM). Chlorophyll concentrations were elevated at both plumes relative to offshore waters, with a median of  $1.9 \pm 0.01$  mg m<sup>-3</sup> around Cape Blanco and  $1.4 \pm 0.01$  mg m<sup>-3</sup> at Cape Mendocino. Both these Chl concentrations

340



345 are well below that which can be supported by the available  $\text{NO}_3^-$  concentrations ( $1 \mu\text{M NO}_3^-$  can typically yield  $1 \mu\text{g chl L}^{-1}$ ), indicating that the phytoplankton blooms were likely in the early phases of development following upwelling.



350 **Figure 3. Variability in SST (a), salinity (b),  $\text{NO}_3^-$  (c), and Chl (d) within the observed water masses offshore, at Cape Blanco, and Cape Mendocino.** The line inside each boxplot represents the median, while whiskers display the 75<sup>th</sup> percentile. Points outside the whiskers represent outliers.

Underway surface measurements were accompanied by on-station discrete sampling for  $\text{NO}_3^-$ ,  $\text{PO}_4$ , Si, and Fe concentrations. As expected,  $\text{NO}_3^-$  was highly correlated with  $\text{PO}_4$  ( $\rho = 0.99$ ,  $p \ll 0.01$ ) and  $\text{SiO}_2$  ( $\rho = 0.92$ ,  $p \ll 0.01$ ). The ratio of  $\text{NO}_3^-:\text{PO}_4$  was  $7.4 \pm 2.0$ , and less than half the expected Redfield ratio of 16. This result is consistent with observations of low  $\text{NO}_3^-:\text{PO}_4$  (~2-3) in the North Pacific attributed to high subsurface denitrification rates (Tyrrell and Law, 1997). In contrast with the strong covariance observed among macronutrients, surface Fe distributions were not correlated with surface  $\text{NO}_3^-$  concentrations ( $\rho = 0.35$ ,  $p = 0.6$ ). At Cape Blanco, Fe concentrations varied from 1.2 – 2.0 nM, whereas Cape Mendocino concentrations were significantly lower, ranging from 0.21 – 0.65 nM. Offshore Fe concentrations were relatively high, with a surface concentration of 0.29-0.42 nM. These waters exhibited low macronutrient concentration. In section 4.1 we explore the potential causes for different nutrient signatures in the various water masses we sampled.

### 3.2 Photo-physiology

365 Along the cruise track, phytoplankton photophysiological properties displayed spatial variability associated with hydrographic gradients, superimposed on significant diel cycles. In particular, we observed strong diel signatures in the expression of various photo-protective mechanisms. We observed decreases in the PSII functional absorption area,  $\sigma_{PSII}$ , throughout the day, followed by recovery overnight (Fig. 4a). The maximum photochemical efficiency of PSII ( $F_v/F_m$ ) similarly decreased during the day and peaked overnight. Measurements of  $\text{NPQ}_{\text{NSV}}$  displayed an inverse diel pattern to those of  $\sigma_{PSII}$  and  $F_v/F_m$ ,



reflecting adjustments to the allocation of absorbed energy between competitive photochemistry and thermal dissipation pathways. These observations agree with previous diel cycle studies of the region (Schuback and Tortell, 2019).

370

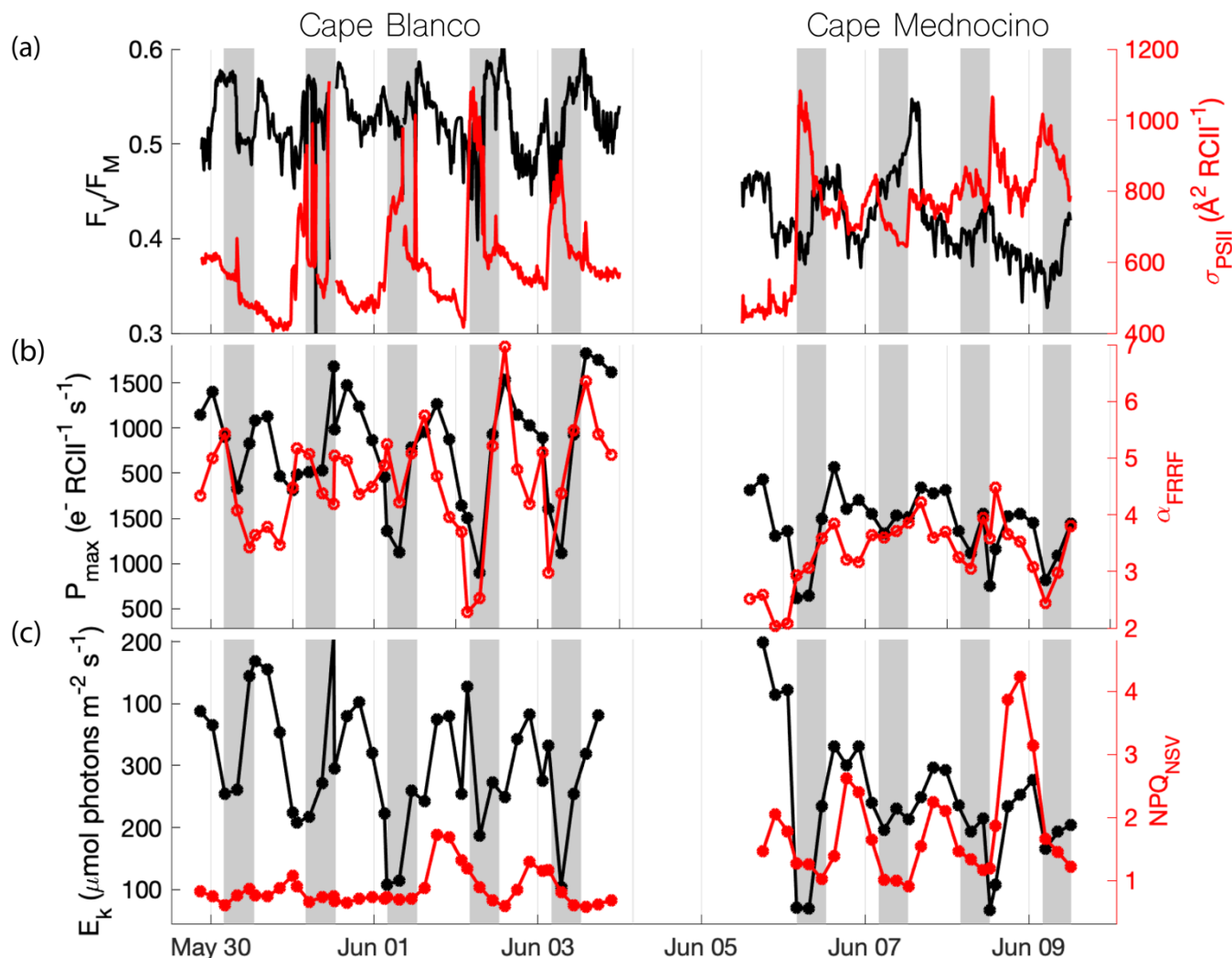


**Figure 4. Diel patterns in photo-physiological properties along the cruise track.** Grey shading indicates night-time, when surface PAR < 5  $\mu\text{mol photons m}^{-2} \text{s}^{-1}$ . **a.**  $F_v/F_M$  (black) and  $\sigma_{PSII}$  (red), **b.**  $P_{\text{max}}$  (black) and  $\alpha$  (red), **c.**  $E_k$  (black) and  $\text{NPQ}_{\text{NSV}}$  (red) are displayed with respect to sampling time. High sea states between 06/04 – 06/06 impacted the seawater intake, resulting in the data gap.

375

Photosynthetic parameters derived from semi-continuous PI curves also exhibited diel patterns that mirrored those of  $F_v/F_M$  and  $\sigma_{PSII}$ . The maximum, light-saturated,  $\text{ETR}_{PSII}$  ( $P_{\text{max}}$ ) and the light utilization efficiency under light limiting conditions ( $\alpha$ ) both peaked during the midday when *in-situ* irradiance was highest. The light saturation level,  $E_k$ , tracked surface light availability, while the photoinhibition parameter ( $\beta$ ) peaked during midday and diminished overnight. As with the continuous underway data, results from these discrete PI curves match the previous diel observations of Schuback and Tortell (2019). We note, however, that there is potential for some convolution of temporal and spatial variability, as the ship spent more time

380



offshore in the night, and on-shore during the daytime. It is thus possible, that some of the diel cycling partially reflects different photo-physiological signals between coastal and offshore waters.

385

Beyond diel signals, we also observed significant gradients in photophysiological parameters in relation to oceanographic conditions. Elevated values of  $F_v/F_m$ ,  $P_{max}$ , and  $\alpha$  were observed in regions of localized upwelling (Table 1), indicating that the vertical transport of nutrient-rich water to the surface supported high photochemical yields. In contrast, signs of upwelling were associated with decreased  $\sigma_{PSII}$  and  $NPQ_{NSV}$ . Notably, the two upwelling plumes (near Cape Blanco and Cape Mendocino) showed significantly different phytoplankton photophysiological properties. At Cape Blanco, mean values of  $NPQ_{NSV}$  and  $\sigma_{PSII}$  were significantly lower than at Cape Mendocino, while  $F_v/F_m$ ,  $P_{max}$ ,  $\alpha$ , and  $\beta$  were all higher at this site, compared to Cape Mendocino (Table 1). Photophysiological properties at Cape Mendocino were much closer to those observed in offshore non-upwelling waters, with mean  $F_v/F_m$  values that were lower than offshore, despite elevated macro-nutrient concentrations. This result, combined with low Fe concentrations at Cape Mendocino, suggests that phytoplankton at Cape Mendocino were Fe-stressed despite the presence of upwelling conditions (see Discussion).

390

395

	CAPE BLANCO	CAPE MENDOCINO	OFF-SHORE	SST N=71604	SAL N=71604	NO <sub>3</sub> <sup>-</sup> N=989	FE N=40	SI N=40	PAR N=71604
$F_v/F_m$ N=1438	0.47±0.01 <sup>A</sup>	0.39 ± 0.08 <sup>B</sup>	0.41± 0.08 <sup>C</sup>	-0.55*	0.27*	0.39*	0.32	0.52	-0.04
$\sigma_{PSII}$ , N=1438	545 ± 5 <sup>A</sup>	655 ± 11 <sup>B</sup>	647 ± 5 <sup>C</sup>	0.58*	-0.38*	-0.45*	-0.55	-0.60	-0.12
$P_{MAX}$ , N=91	977±83 <sup>A</sup>	600 ± 42 <sup>B</sup>	600 ± 91 <sup>B</sup>	-0.67*	0.40*	0.50*	0.45	0.78*	0.19
$\alpha$ , N=91	4.8±0.3 <sup>A</sup>	3.3 ± 0.3 <sup>B</sup>	3.6 ± 0.4 <sup>B</sup>	-0.57*	0.19	0.24	0.37	0.45	-0.11
$E_k$ , N=91	210±19 <sup>A</sup>	172 ± 20 <sup>B</sup>	176 ± 15 <sup>B</sup>	-0.38*	0.33*	0.41*	0.62	0.72*	0.37*
$NPQ_{NSV}$ , N=91	0.75±0.05 <sup>A</sup>	1.33 ± 0.2 <sup>B</sup>	1.2 ± 0.2 <sup>B</sup>	0.66*	-0.26	-0.46	-0.36	-0.62	0.58*

**Table 1. Summary of photophysiological properties at each sampling environment and their relationship to hydrographic parameters.** Left side of the table displays the median ± median absolute deviation for each photophysiological parameter according to sampling environment. Superscripts denote groups with significantly different medians. Right side of the table displays spearman rank correlation coefficients for each photophysiological parameter against environmental parameters. \* indicates  $p < 0.05$ . Due to differences in sampling frequencies, the number of observations (N) varied across different parameters. For correlation analyses, paired observations were matched in space and time to the lowest resolution measurement.

400

405

### 3.3 Primary Productivity

#### 3.3.1 Electron Transport Rates, $ETR_{PSII}$

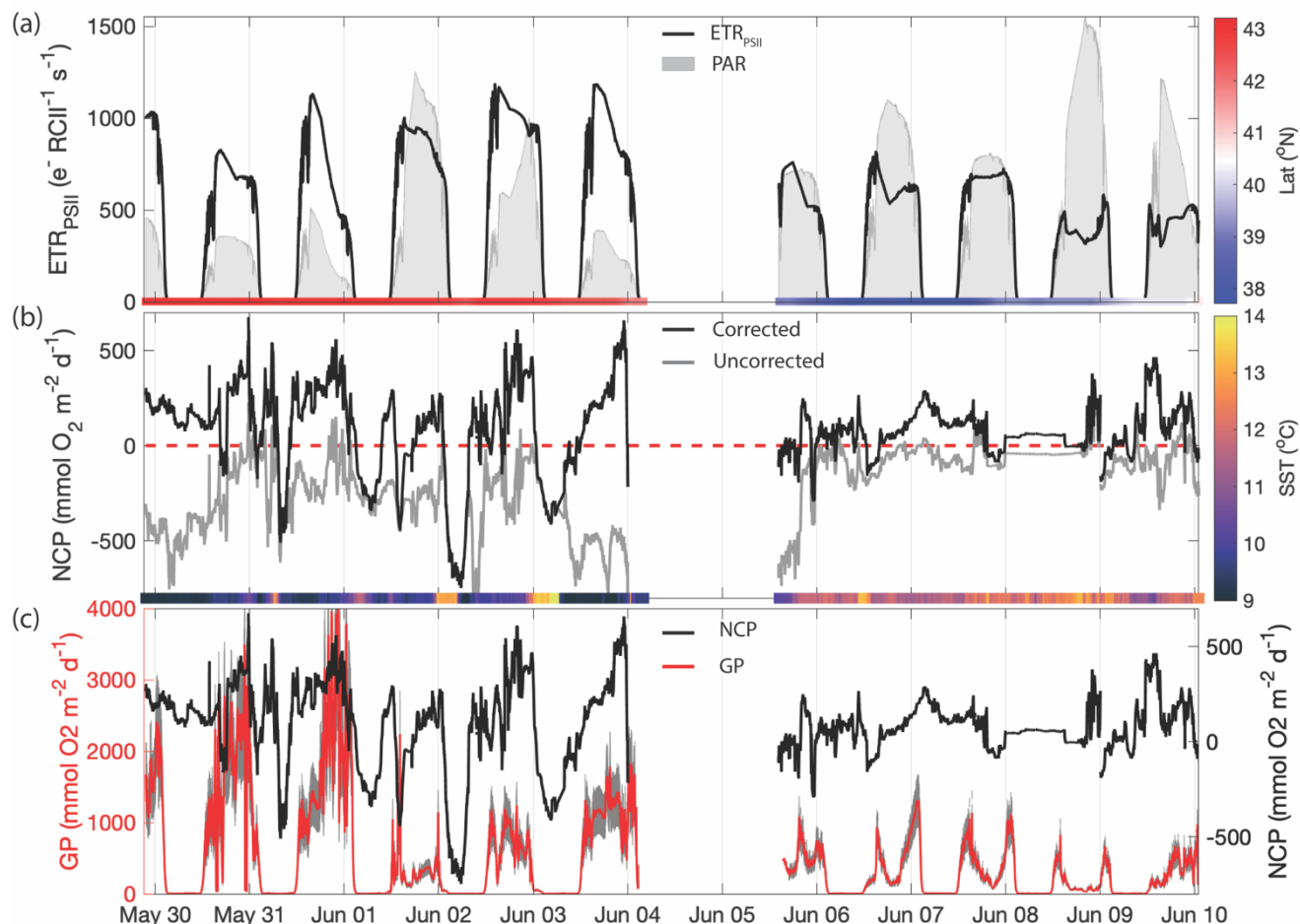
In-situ  $ETR_{PSII}$ , followed a notable diel cycle due to its first order dependency on irradiance (Eq 1, Fig. 5a). However, the relationship between PAR and  $ETR_{PSII}$  was spatially variable across the cruise track, reflecting differences in  $\alpha_{FRFF}$ ,  $P_{max}$ , and  $E_k$  between Cape Blanco and Cape Mendocino (Table 1; Fig. 4). The amplitude of diel  $ETR_{PSII}$  was greatest near Cape Blanco, despite lower average mixed layer PAR (Fig 4a). At Cape Blanco, maximum ETR averaged  $977 \pm 83 \text{ e}^- \text{ RCII}^{-1} \text{ s}^{-1}$ , as compared

410





to maximum values of only  $600 \pm 42 \text{ e}^- \text{ RCII}^{-1} \text{ s}^{-1}$  at Cape Mendocino. The higher maximum ETR at Cape Blanco is in good agreement with the observations of higher photochemical yields in this region (Table 1).



415 **Figure 5. Primary productivity time series along the cruise track. a)** ETR<sub>PSII</sub> derived from FRRF-measured PI curve  
 420 parameter interpolated to match NCP sampling frequency (black line). The grey patches indicate the mean PAR available  
 within the mixed layer. The bar on the bottom is coloured by the sampling latitude. The Cape Blanco filament is designated as  
 latitude > 40.5 and is coloured red, while Cape Mendocino is designated as latitude < 40.5 coloured blue. **b)** Uncorrected NCP  
 (grey) and mixing-corrected NCP (black). The dashed red line denotes the boundary between net autotrophy (NCP > 0) and  
 net heterotrophy (NCP < 0). The color bar on the bottom illustrates the sample temperature. **c)** mixing-corrected NCP (black,  
 right y-axis) and gross photochemistry (GP), shown in red (left y-axis). GP is calculated by converting ETR<sub>PSII</sub> from units e<sup>-</sup>  
 RCII<sup>-1</sup> s<sup>-1</sup> to mmol O<sub>2</sub> m<sup>-2</sup> d<sup>-1</sup>. The grey shading around the red line displays the range of GP based on an assumed range of 400  
 – 700 Chl:RCII.

### 3.3.2 Net Community Productivity, NCP

425 In addition to GPP, we estimated NCP from underway measurements. Prior to correcting for vertical mixing, more than 80%  
 of derived NCP values were less than 0, suggesting net heterotrophic conditions over most of the cruise track. The most



negative uncorrected NCP values were observed near Cape Blanco, despite the high gross photochemistry rates measured in this region.

- 430 The apparent decoupling between NCP and GPP can be largely explained by vertical mixing of low O<sub>2</sub> waters, which artificially depress O<sub>2</sub>-derived NCP estimates (see Sect. 2.4). After applying the N<sub>2</sub>O-based mixing correction, we found that the majority of the cruise track (73% of measurements) exhibited net autotrophy, with the highest value recorded within the Cape Blanco filament. For the most part, net heterotrophy only existed at night in warmer off-shelf waters. The mean corrected NCP was  $80 \pm 218$  mmol O<sub>2</sub> m<sup>-2</sup> d<sup>-1</sup>, within range of previous observations of late-spring NCP within the California Current
- 435 (Kranz *et al.*, 2020). The large standard deviation reflects the large diel and spatial variability observed along the cruise track. The highest NCP estimates we obtained ( $> 500$  mmol O<sub>2</sub> m<sup>-2</sup> d<sup>-1</sup>) are on the upper end of previous measurements. Values above 100 mmol O<sub>2</sub> m<sup>-2</sup> d<sup>-1</sup> have only been observed in the most productive coastal waters (Wang *et al.*, 2020; Niebergall *et al.*, 2023), further emphasizing the high productivity of the CCS.
- 440 The N<sub>2</sub>O-derived mixing correction term was strongly correlated to N<sub>2</sub>O-independent indicators of upwelling, namely temperature ( $\rho = -0.77$ ,  $p \ll 0.01$ ). These results give confidence that high surface concentrations of N<sub>2</sub>O are a valid marker of upwelling and transport of O<sub>2</sub>-poor subsurface water into the mixed layer. The maximum correction factor, 1200 mmol O<sub>2</sub> m<sup>-2</sup> d<sup>-1</sup>, was observed within the cold upwelling filament near Cape Blanco, where uncorrected NCP was below -500 mmol O<sub>2</sub> m<sup>-2</sup> d<sup>-1</sup>. This result highlights the impact of vertical fluxes on O<sub>2</sub>-based NCP estimates in upwelling regions.

### 445 3.3.3 Carbon fixation rates

At nine discrete sampling stations, <sup>14</sup>C-based PI curves were measured in parallel with ETR<sub>PSII</sub> at the surface and at the base of the euphotic zone. Volumetric carbon fixation rates varied significantly between stations and depths. Maximum carbon fixation rates (carbon-based P<sub>max</sub>) ranged from 0.4 to 96 μg C L<sup>-1</sup> hr<sup>-1</sup>. Over 85% of the variability in carbon fixation rates could be explained by differences in biomass, which varied from 0.11 to 9 mg Chl L<sup>-1</sup>. Chlorophyll concentrations in near-

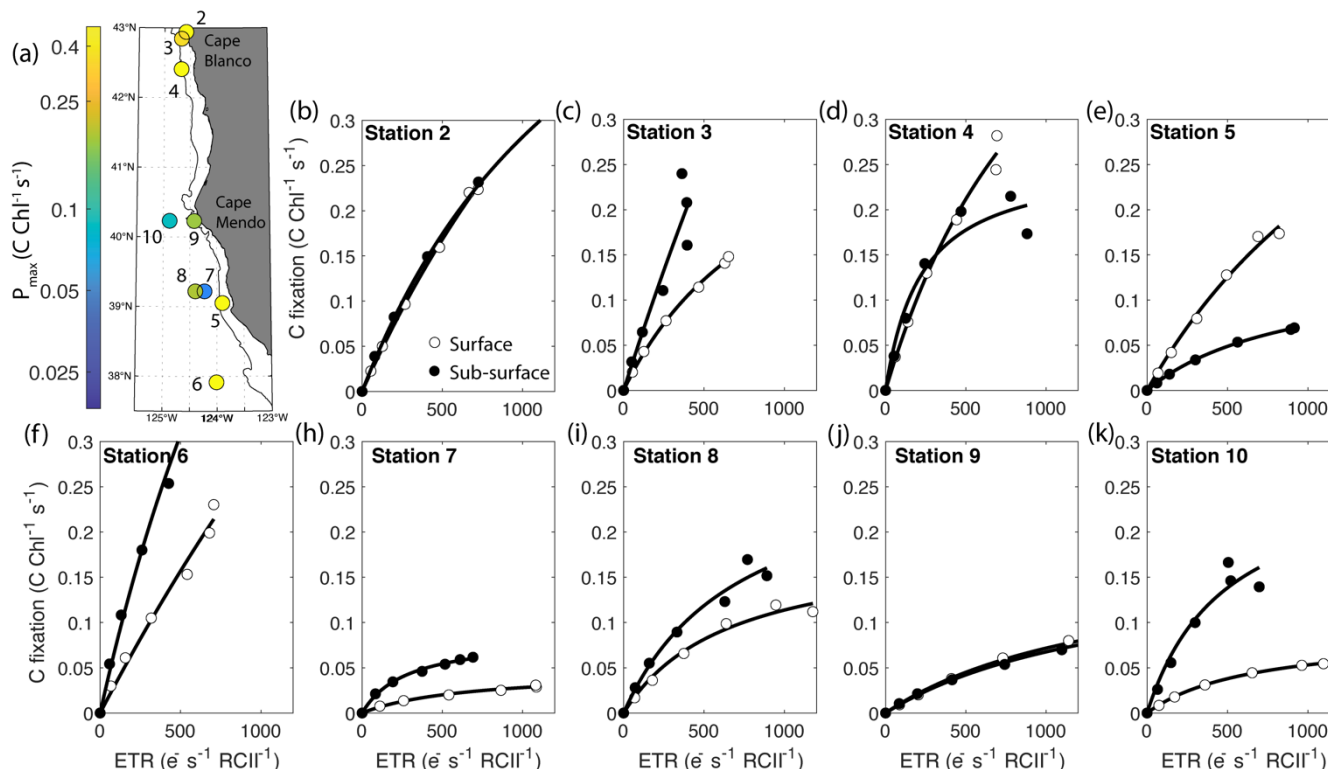
450 surface waters were, on average, four times higher than those at the base of the euphotic zone, implying the bulk of carbon fixation took place in the mixed layer. The bottom depth of the euphotic zone was  $x \pm y$  times greater, on average, than the bottom depth of the mixed layer.

To compare carbon-based GPP estimates against parallel ETR<sub>PSII</sub> measurements, carbon fixation rates were normalized to chlorophyll and converted to units of C chl<sup>-1</sup> s<sup>-1</sup>. Chlorophyll normalized carbon fixation rates were positively correlated with Fe ( $\rho = 0.40$ ,  $p < .05$ ), F<sub>v</sub>/F<sub>M</sub> ( $\rho = 0.56$ ,  $p < .05$ ), and Si:NO<sub>3</sub><sup>-</sup> ratios ( $\rho = 0.60$ ,  $p < .05$ ), and negatively correlated with  $\sigma_{PSII}$  ( $\rho = -0.68$ ,  $p < .05$ ). These results suggest that stations with low chlorophyll-normalized carbon fixation rates may have been affected by Fe and Si co-limitation. By comparison, carbon fixation rates were not significantly correlated with NO<sub>3</sub><sup>-</sup> or PO<sub>4</sub> concentrations or salinity.

460 Notably, carbon fixation consistently saturated at lower light intensities than ETR<sub>PSII</sub>. The average E<sub>k</sub> for ETR<sub>PSII</sub> was  $5 \pm 2.8$  times greater than E<sub>k</sub> for carbon fixation. As a result, carbon fixation did not scale linearly with ETR<sub>PSII</sub>, but rather demonstrated a hyperbolic relationship at each station and depth sampled. At sub-saturating light levels, carbon fixation increased linearly with ETR<sub>PSII</sub>, until approaching an asymptote as ETR<sub>PSII</sub> continued to increase while carbon-fixation remained stationary (Fig

465 6). This result indicates that at light levels beyond the saturating index for carbon-fixation, ETR<sub>PSII</sub> provides reducing power in excess Calvin-Benson Cycle requirements. Previous studies have noted a similar nonlinear relationship between carbon fixation and ETR<sub>PSII</sub>, consistent with an upregulation of alternative electron pathways under high light levels (Suorsa, 2015; Zhu *et al.*, 2017; Schuback and Tortell, 2019). This non-linear relationship between C fixation and ETR has been cited as a key limitation to the widespread use of FRRF for autonomous high resolution GPP estimates. Although our results demonstrate

470 a clear hyperbolic relationship between these rates, the parameters describing this relationship were variable across stations. In sect. 4.3, we further examine the relationship between carbon fixation and ETR<sub>PSII</sub>, and contextualize the apparent differences in carbon-electron decoupling with available physiological, and environmental data.



475

**Figure 6. Parallel measurements of fluorescence- and  $^{14}\text{C}$ -based photosynthesis-irradiance experiments conducted on-station.** The top left displays the sample locations coloured by maximum chl-specific surface carbon fixation rates. The black contour line displays the 200m isobath. The other panels show carbon fixation rates plotted against  $\text{ETR}_{\text{PSII}}$ . Surface samples are represented by open circles while sub-surface samples are depicted as closed circles. Each curve is fit with the function,  $C \text{ fixation} = \frac{C_{\text{max}} \cdot \text{ETR}_{\text{PSII}}}{K_{\text{sat}} + \text{ETR}_{\text{PSII}}}$ , where  $C_{\text{max}}$  is the maximum carbon fixation rate, and  $K_{\text{sat}}$  is the saturation constant beyond which changes in carbon fixation with respect to  $\text{ETR}_{\text{PSII}}$  become increasingly non-linear. Carbon fixation data were not collected at Station 1. All curve fits had an  $R^2 > 0.9$ .

480

#### 4 Discussion

485

As expected, our continuous underway measurements revealed strong spatial and temporal variability in biogeochemical properties across the California Upwelling system. In particular, we observed large diel cycles, and coastal-offshore gradients in biogeochemical properties, with two distinct upwelling filaments in the vicinity Cape Mendocino and Cape Blanco. Differences in nutrient availability between sample sites appeared to exert a strong influence on photo-physiology, gross photochemistry, gross primary productivity and net community productivity. In this section, we explore the potential underlying causes of biogeochemical differences across our survey region, with a focus on iron gradients across the two distinct upwelling filaments. We also discuss the direct and indirect influence of iron availability and other environmental variables on phytoplankton photo-physiology, and energy transfer efficiencies between photosynthetic processes.

490



#### 4.1 Factors driving the contrasting biogeochemistry of Cape Blanco and Cape Mendocino filaments

495 The significant differences in surface oceanographic conditions between upwelling filaments may have been driven by differences in 1) the strength and timing of upwelling at the two Capes, or 2) differences in the nutrient content of the sub-surface upwelling source waters. We investigated these two possibilities by examining the NOAA coastal upwelling transport index (CUTI) as a proxy for upwelling strength during and prior to the sampling period, and by evaluating nutrient depth profiles to examine the upwelling source waters at the two capes. Our analysis suggests that both factors likely contributed to the apparent differences between Cape Blanco and Cape Mendocino biogeochemistry, providing evidence that Fe and Si concentrations were particularly affected by bathymetric features that influence Fe supply.

##### 500 4.1.1 Strength of upwelling and relative age of filaments

To examine differences in the timing and strength of upwelling between the two filaments, we tracked CUTI for a 10 day interval prior to sampling (Jacox *et al.*, 2018). Throughout the sampling period, the strength of upwelling at Cape Blanco varied from 1.3 to 2.4 m d<sup>-1</sup> of vertical transport (positive values indicate upwelling) and peaked 6 days prior to our arrival, when vertical transport rates were 3.8 m d<sup>-1</sup>. During our sampling period at Cape Mendocino, vertical transport varied from -0.2 to 3.3 m d<sup>-1</sup>. Upwelling conditions persisted in this region, with vertical transport rates > 2 m d<sup>-1</sup> between June 1 and 4, four to one days prior to our arrival. However, after June 4, the vertical mixing index at Cape Mendocino rapidly reversed to weak downwelling (-0.1 to -0.3 m d<sup>-1</sup>) during the last few days of sampling, emphasizing the dynamic nature of this sampling environment. These results support the hypothesis that colder and more nutrient rich water near Cape Blanco was attributable to stronger and more consistent upwelling in this region in the interval prior to our sampling. In contrast, Cape Mendocino was transitioning from upwelling to downwelling during our sampling period.

##### 510 4.1.2 Nutrient Content of upwelling source waters

Nutrient depth profiles offer additional insight into the nutrient concentrations of upwelling filament source waters. Unfortunately, nutrient samples were only collected down to the base of the euphotic zone, missing the deeper source waters. Nonetheless, measurements at the base of the euphotic zone (40-50m) enable us to compare subsurface nutrient concentrations. 515 Mean concentrations of [NO<sub>2</sub><sup>-</sup> + NO<sub>3</sub><sup>-</sup>] between 40 and 50m were significantly ( $p < 0.05$ ) higher at Cape Blanco ( $24.5 \pm 4.3 \mu\text{M}$ ) than at Cape Mendocino ( $16.5 \pm 5.7 \mu\text{M}$ ). Similarly, phosphate concentrations between 40-50m were significantly greater around Cape Blanco ( $2.6 \pm 0.3 \mu\text{M}$ ) compared to Cape Mendocino ( $2.1 \pm 0.4 \mu\text{M}$ ;  $p = 0.02$ ). Relative to nitrate and phosphate, larger differences were observed in Fe and Si concentrations between the two capes. The 40-50m silicic acid concentration at Cape Blanco ( $30.0 \pm 8.6 \mu\text{M}$ ) was nearly double that observed at Cape Mendocino ( $16.3 \pm 8.2 \mu\text{M}$ ;  $p \ll 520 0.01$ ), while, Fe concentrations between 40-50m at Cape Blanco ( $6.8 \pm 4.1 \text{ nM}$ ) were more than three-fold higher than those at Cape Mendocino ( $1.8 \pm 2.3 \text{ nM}$ ;  $p = 0.01$ ). These results support the hypothesis that the two upwelling plumes were seeded by different water masses with distinct nutrient concentrations.

Differences in underlying bathymetric features between Cape Blanco and Mendocino likely contributed to the observed 525 differences in Fe and Si availability. Cape Blanco sits over a broad section of the continental shelf (> 30km wide) composed of highly erodible sedimentary rocks with mineral rich sand-silt layers originating from the Klamath Mountains (Spigai, 1971). The broad shelf continues south until the triple junction of the North American, Pacific, and Gorda plates which forms the submarine Mendocino escarpment, a narrow ridge extending west from Cape Mendocino along the transform fault (Menard and Dietz, 1952). Importantly, the shelf rapidly narrows to less than 5 km at the latitude of Cape Mendocino (Appendix 1). 530 Differences in shelf width have important implications on sub-regional iron availability. Previous work by Biller *et al.* (2013) demonstrated that shelf width correlated with greater Fe bioavailability in the water layer directly overlying the seafloor. This trend was evident in our study as well, with a  $\rho = 0.57$  correlation between shelf width and Fe concentrations at the bottom of the euphotic zone for on-shelf stations. Yet, with only nine stations on-shelf stations, this correlation was not statistically significant.



535

In contrast with  $\text{NO}_3^-$  and  $\text{PO}_4^{3-}$ , which are resupplied to the surface by upwelling, remineralized Fe is rapidly removed from the water column, such that Fe supply to the surface can be significantly decoupled from macronutrients (King and Barbeau, 2011; Bruland, Middag and Lohan, 2014). As a result, differences in upwelling strength at Cape Blanco and Cape Mendocino likely account for the differences in  $\text{PO}_4^{3-}$  and  $\text{NO}_3^-$  between the two sites, while contrasting shelf features can explain the larger differences in Fe availability. These observations fit within the theory that the California Current contains a ‘mosaic’ of Fe limitation, where patches of Fe-poor water may persist even in the presence of upwelling conditions (Hutchins *et al.*, 1998; Till *et al.*, 2019). In the following section, we present several lines of evidence that photo-physiological properties of phytoplankton assemblages were influenced by iron gradients.

540

#### 4.2 Environmental and taxonomic influences on physiology and productivity

545

Environmental gradients exert strong effects on physiology and productivity by determining the supply of essential nutrients that support phytoplankton growth and the maintenance of photosynthetic proteins. As a cofactor in many biological redox reactions, Fe plays a particularly important role in the photosynthetic electron transport chain and nutrient uptake pathways. Several lines of evidence suggest that iron stress was a key factor shaping phytoplankton productivity and photo-physiology across our study site. As noted above, there was a significant difference in Fe concentrations between Cape Blanco (high Fe) and Mendocino (low Fe) associated with variability in the shelf width. The difference in Fe-availability was strongly correlated with  $\text{Si:NO}_3^-$  ( $\rho = 0.85$ ,  $p \ll 0.0.1$ ), likely reflecting excess Si uptake by iron-limited diatoms (M. Franck *et al.*, 2000; Sarthou *et al.*, 2005). Further evidence of Fe-stress at Cape Mendocino was obtained from ancillary transcriptomic analysis, which demonstrated elevated expression of the Fe assimilation gene *Feal* (Appendix 3), which has previously been cited as a marker of Fe-stress (Allen *et al.*, 2007). Together, these observations indicate the onset of Fe stress at sites with reduced Fe-availability. Below we outline the apparent taxonomic and physiological responses to apparent Fe stress.

550

555

Beyond directly affecting phytoplankton physiology, Fe gradients can indirectly influence phytoplankton physiology and productivity by driving taxonomic shifts towards species that are adapted to low Fe conditions. After chlorophyll, the second most abundant pigment across the cruise track was diatom-specific fucoxanthin, indicating that our sampling region was dominated by diatoms (Appendix 2). Microscope cell counts confirmed that diatoms were the most abundant taxa, with the majority of cells belonging to the genus *Chaetoceros*. Although diatoms were the most dominant group across the study area, their relative contribution was significantly lower around Cape Mendocino compared to Cape Blanco. Moreover, we observed a taxonomic shift towards smaller phytoplankton around Cape Mendocino, including smaller diatoms and dinoflagellates. Smaller cells sizes afford larger surface area to volume ratios, facilitating nutrient uptake at lower concentrations (Sunda and Huntsman, 1997). Stations near Cape Mendocino were characterized by high abundances of *Pseudo-nitzschia*, which were absent from Cape Blanco. *Pseudo-nitzschia* is a well-studied diatom with a number of physiological adaptations to Fe-limitation, causing it to be favoured over other diatoms under low Fe conditions (Lampe *et al.*, 2018). These shifts in phytoplankton assemblages towards smaller sizes and low Fe specialists suggest bottom-up environmental controls driving taxonomic composition.

560

565

570

Cell size and nutrient status influence the optical properties and photo-physiology of phytoplankton. Large cells are prone to pigment packaging effects, which decrease Chl-specific absorption as intracellular Chl concentrations increase and surface area to volume ratios decrease. This effect causes reduced  $\sigma_{PSII}$ , as was observed near Cape Blanco (Table 1). Nutrient limitation, particularly for Fe, is associated with photo-inactive or damaged RCII (Roncel *et al.*, 2016). Inactive RCII still absorb light, but do not contribute to photochemistry. This, in turn, drives high  $\sigma_{PSII}$ , which is proportional to the light harvesting complex absorption coefficient normalized by active RCII concentrations (Oxborough *et al.*, 2012; Li *et al.*, 2021), and low  $F_v/F_m$ , due to inactive RCII contributing to the  $F_m$  but not  $F_v$  signal (Schuback, Philippe D Tortell, *et al.*, 2021). Both of these commonly cited indicators of Fe stress were observed around Cape Mendocino and also offshore (Table 1).

575

580

The taxonomic and nutrient-dependent effects on photo-physiology described above are expected to directly impact  $\text{ETR}_{PSII}$  (Eq. 1). Previous studies have noted higher  $\text{ETR}_{PSII}$  among Fe-limited phytoplankton, presumably due to increased  $\sigma_{PSII}$





585 (Schuback *et al.*, 2015). However, we observed greater  $ETR_{PSII}$  in the relatively Fe-rich waters near Cape Blanco (Table 1), likely due to high  $F'_q/F'_v(PAR)$ , which represents the proportion of open RCII at a given light level (Suggett, Moore and Geider, 2011). Low NPQ observed in the Cape Blanco region (Fig. 4d) likely enabled  $F'_q/F'_v$  to remain high under high light levels. It is well recognized that iron limitation exacerbates high light stress and NPQ (Ryan-keogh *et al.*, 2020; Schallenberg *et al.*, 2020), and the high NPQ at Cape Mendocino compared to Cape Blanco provides further evidence that Cape Mendocino assemblages were affected by Fe stress. Iron limitation can also impact photosynthetic processes downstream of  $ETR_{PSII}$ . In this study, maximum carbon fixation rates ( $P_{max}$  determined during  $^{14}C$  PI experiments) displayed a strong correlation with Si ( $\rho = 0.63, p \ll 0.0.1$ ) and the ratio of Si:NO $_3^-$  ( $\rho = 0.60, p \ll 0.0.1$ ) in the water column.

590 Overall, our results suggest that Fe availability gradients between Cape Blanco and Mendocino influenced local community composition and physiology with consequential effects on C and Si cycles. Differences in taxonomic composition, photo-physiology, nutrient quotas and productivity all serve as evidence that the community shifted towards Fe-limitation in proximity to Cape Mendocino. Due to the differential sensitivity of  $ETR_{PSII}$ , carbon fixation, and NCP to Fe-availability, we 595 hypothesized that Fe-limitation would lead to a decoupling between these different PP currencies. We explore this hypothesis below with direct comparisons of  $ETR_{PSII}$ , C-fixation, and NCP.

### 4.3 Energy transfer efficiencies between photosynthetic processes

600 Measurements of primary productivity in different ‘currencies’ (carbon, oxygen and electrons) each reflect the rates of different photosynthetic processes. Comparison of these alternative productivity metrics thus yields information on energy transfer efficiencies across different components of the photosynthetic pipeline (Fig 7). Theoretically, water-splitting and carbon fixation have fixed stoichiometries, with 4 charge separation events required to produce one O $_2$  and fix one CO $_2$ . Yet a number of non-linear electron transport pathways divert reducing power from carbon fixation, decoupling  $ETR_{PSII}$  from GPP (Fig 7). Oxygen consumption by respiration and non-linear electron transport pathways further decouple  $ETR_{PSII}$  from O $_2$  fluxes and NCP. The ratio between  $ETR_{PSII}$  and GPP thus provides information on the magnitude of non-linear electron transport, while 605 the ratio between  $ETR_{PSII}$  and NCP reflects the sum of non-linear electron transport and respiration. In practice, interpreting apparent decoupling between ETR, GPP, and NCP is complicated by differences in the temporal and spatial scales captured by different measurement approaches, as well as the various assumptions implicit in each method. In the following sections, we directly compare parallel productivity measurements to examine energy transfer efficiencies across photosynthetic processes, taking care to note important methodological considerations.

610

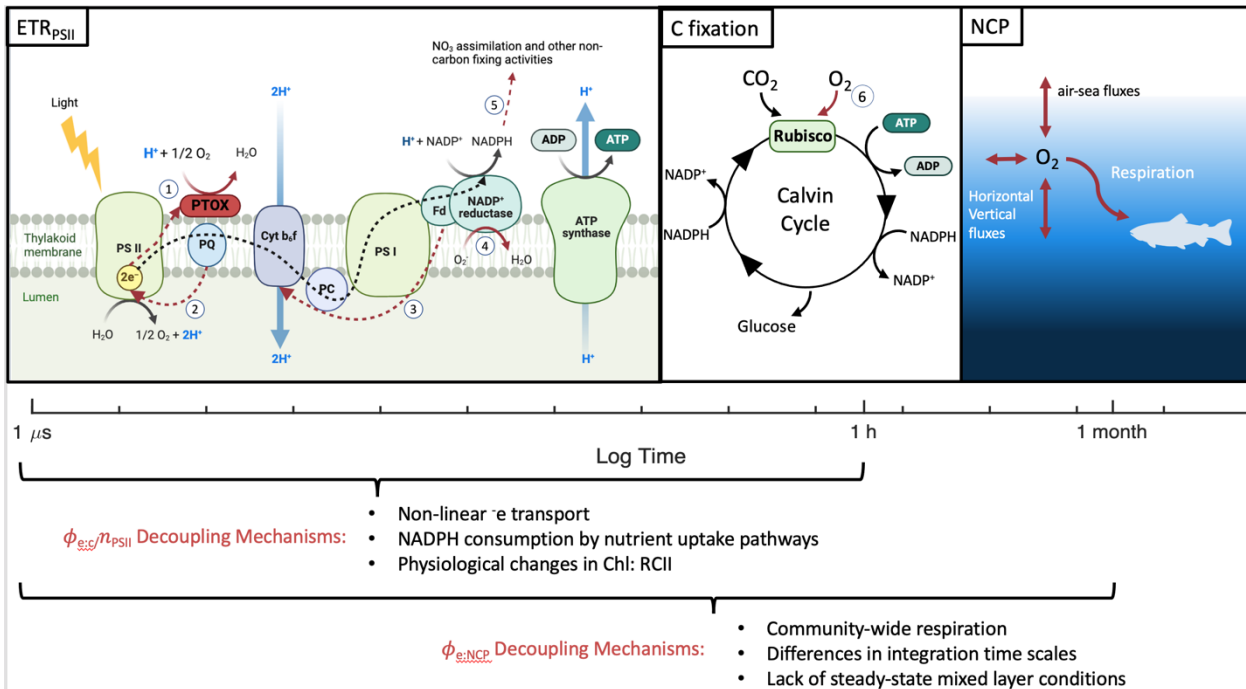


**Figure 7. Different primary productivity currencies and their decoupling mechanisms.** The three productivity currencies of interest are indicated with respect to the spatial times scales they represent. Numbered red pathways denote decoupling mechanisms including 1) photorespiration 2) cyclic transport around PSII 3) cyclic transport around PSI 4) pseudo-cyclic/ Mehler reactions 5) reductant consuming nutrient uptake pathways 6) chloro-respiration and 7) Community-wide respiration. Figure produced in Biorender.

### 4.3.1 Carbon fixation as a function of ETR<sub>PSII</sub>

Non-linear electron transport pathways (Fig 7) maintain redox homeostasis when ETR<sub>PSII</sub> exceeds downstream energy requirements for growth and metabolism. The energy balance between PSII and PSI becomes disrupted under high irradiance, when PSII absorbs energy in excess of PSI electron transport rates, and/or under nutrient limitation, limiting the synthesis of electron transporters (Schuback, Schallenberg, Duckham and Maldonado, 2015; Roncel *et al.*, 2016; Hughes, Varkey, *et al.*, 2018). Iron limitation, in particular, exerts acute constraints on the synthesis of Photosystem I (PSI) and Cytochrome b<sub>6</sub>/f (Cyt b<sub>6</sub>/f), which require 12 and 5 Fe atoms each (Raven, Evans and Korb, 1999). As a result, Fe-limited phytoplankton have high levels of PSII relative to PSI, exacerbating energy imbalances between PII and PSI, and necessitating upregulation of non-linear electron transport pathways (Behrenfeld and Milligan, 2013). We therefore hypothesized that Fe-stress would increase decoupling between C-fixation and ETR<sub>PSII</sub>.

One of the primary findings of this work is that C-fixation varies as a hyperbolic function of ETR<sub>PSII</sub>. Curve shapes, defined by the maximum carbon fixation rate (P<sub>max-C</sub>) and the saturation constant (K<sub>sat</sub>), were highly variable between samples (Fig. 6). Samples with high P<sub>max-C</sub> and K<sub>sat</sub>, (e.g. Station 6) showed more linear relationships between C-fixation and ETR<sub>PSII</sub>, and had a nearly constant electron requirement for carbon fixation ( $\phi_e : c/n_{PSII}$ , units = e<sup>-</sup> Chl C<sup>-1</sup> RCII<sup>-1</sup>), indicating tightly coupled ETR<sub>PSII</sub> and carbon fixation (Fig 8). By contrast, in samples with low P<sub>max-C</sub> and K<sub>sat</sub>, carbon-fixation quickly saturated with respect to ETR<sub>PSII</sub>, resulting in an increase in  $\phi_e : c/n_{PSII}$  with increasing light levels (e.g. Station 7). Determining sources of P<sub>max-C</sub> and K<sub>sat</sub> variability therefore provides significant utility in predicting the stoichiometry of electron requirements for



gross carbon fixation. This stoichiometry, represented by  $\phi_e:c/n_{PSII}$ , is necessary to derive GPP in ecologically-relevant carbon units from fluorescence-based  $ETR_{PSII}$  measurements.

640 Previous studies have documented the importance of different environmental, taxonomic and physiological parameters in driving variability in  $\phi_e:c/n_{PSII}$ , but efforts to develop empirical algorithms predicting  $\phi_e:c/n_{PSII}$  remain ongoing. Recent studies have used  $NPQ_{NSV}$  to predict  $\phi_e:c/n_{PSII}$ , based on the rationale that NPQ responds directly to excess excitation pressure, which is also expected to stimulate non-linear electron transport. Recently, Schuback *et al.*, (2015, 2016, 2017) noted a consistent relationship between  $NPQ_{NSV}$  and  $\phi_e:c/n_{PSII}$  in the surface waters of the Northeast Pacific and Canadian Arctic, suggesting that carbon fixation can be estimated using FRRF-based NPQ and  $ETR_{PSII}$  measurements alone. Subsequent studies

645 have applied the  $NPQ_{NSV} \propto \phi_{e:c}/n_{PSII}$  relationship observed by Schuback *et al.* (2015) to collect high-resolution fluorescence-based GPP estimates, e.g. Kranz *et al.* (2020). Others, however, have noted that the  $NPQ_{NSV} \propto \phi_{e:c}/n_{PSII}$  relationship does not hold for all taxa (Hughes *et al.*, 2021), light conditions (Schuback *et al.*, 2017), or environments where phytoplankton grow on more reduced N forms like  $NH_4^+$  (Fei *et al.*, 2024).

650 In our study,  $NPQ_{NSV}$  was positively correlated with  $\phi_{e:c}/n_{PSII}$  ( $\rho = 0.55, p \ll 0.01$ ). However, the linear relationship proposed by Schuback *et al.* (2017; 2019) did not adequately predict  $\phi_{e:c}/n_{PSII}$  for our samples ( $R^2 = -0.41$ ), nor did we find a single line of best fit that could describe all of our data ( $R^2 = 0.30$ ). Rather, we found that  $\phi_{e:c}/n_{PSII}$  scaled directly with  $NPQ_{NSV}$  only for samples with low  $C_{max}$  ( $\leq 0.3 \text{ C Chl}^{-1} \text{ s}^{-1}$ ). In contrast, for samples with high  $P_{max-C}$  ( $> 0.3 \text{ C Chl}^{-1} \text{ s}^{-1}$ ),  $\phi_{e:c}/n_{PSII}$  remained relatively constant across increasing light,  $NPQ_{NSV}$ , and  $ETR_{PSII}$  (Fig 8).

655

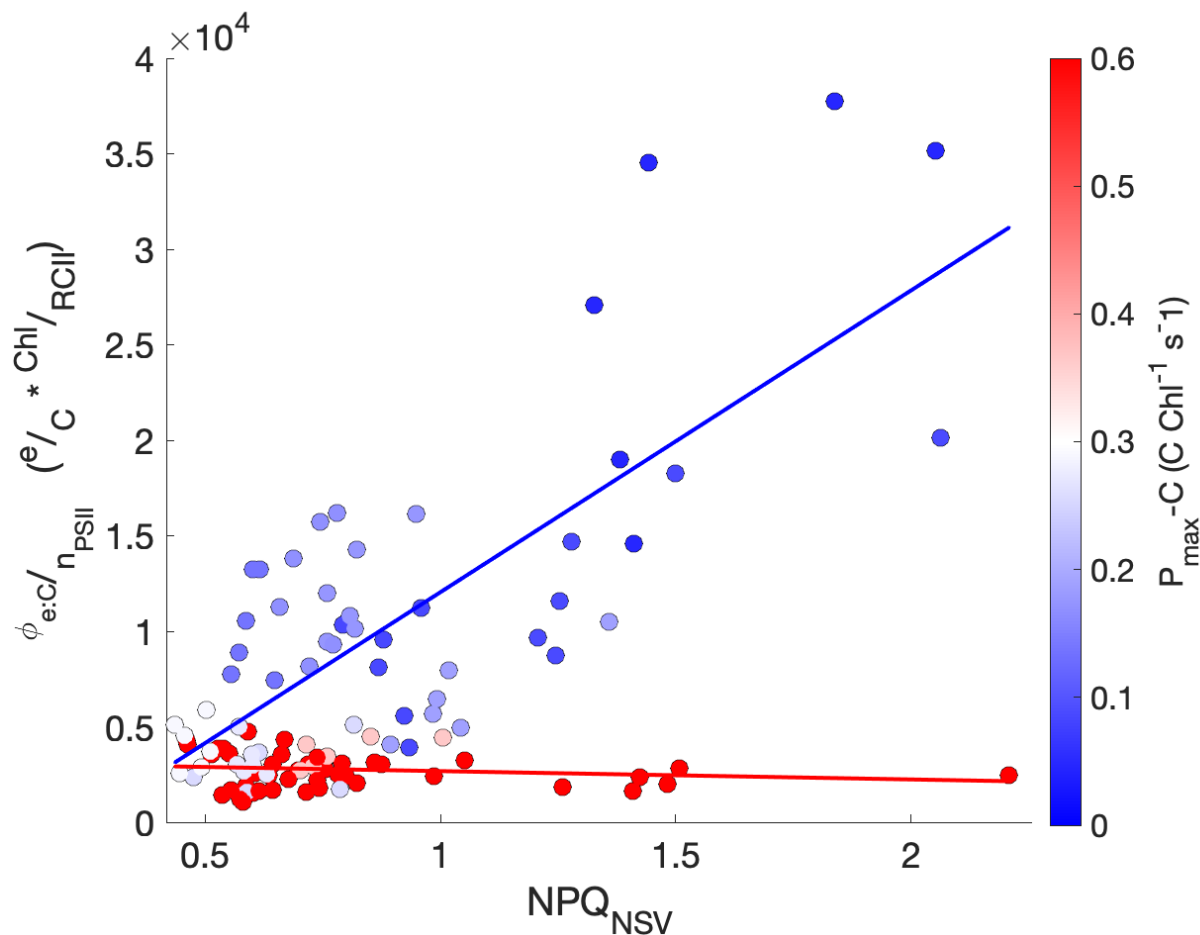




**Figure 8. The relationship between  $\phi_e$ :C, NPQ<sub>NSV</sub> and  $V_{\max}$ .** Lines of best fit are drawn through points with  $P_{\max}\text{-C} \leq 0.3$  and  $> 0.3$  mol C mol Chl<sup>-1</sup> s<sup>-1</sup>, with the colorbar indicating  $P_{\max}\text{-C}$ .

660 The hyperbolic function used to fit  $\text{ETR}_{\text{PSII}}$  and carbon fixation data is equivalent to the Michaelis-Menten equation commonly  
used to describe enzyme kinetics data. By analogy with the enzyme kinetics model, variability in  $P_{\max}\text{-C}$  can be explained as  
the product of the enzyme concentration and maximum reaction rate (Choi, Rempala and Kim, 2017). In our case,  $P_{\max}\text{-C}$   
reflects the entire suite of proteins that facilitate the conversion of chemical energy to organic matter. Reduced concentrations  
of PSI and Cyt b<sub>6</sub>f expected under Fe-stress would therefore reduce  $P_{\max}\text{-C}$ . Consistent with this hypothesis,  $V_{\max}$  was  
665 significantly correlated to physiological markers of Fe-stress,  $\sigma_{\text{PSII}}$  ( $\rho = -0.68$ ,  $p \ll 0.01$ ),  $F_v/F_m$  ( $\rho = 0.56$ ,  $p = 0.02$ ), and  
Si:NO<sub>3</sub><sup>-</sup> ( $\rho = 0.60$ ,  $p = 0.01$ ). Additionally, meta transcriptomic analysis of diatom RNA revealed significant positive  
correlations ( $p < 0.05$ ) between  $P_{\max}\text{-C}$  and the expression level of different PSI subunits (*psaE*, *psaL*, *psaM*), with correlation  
coefficients of  $\rho = 0.71$ ,  $0.70$ , and  $0.93$ , respectively. In contrast, there were no detected correlations between  $P_{\max}\text{-C}$  and Cyt  
b<sub>6</sub>f, however *Cyt b559a*, a subunit of PSII thought to be involved in photoprotection (Burda *et al.*, 2003), also demonstrated a  
670 strong positive correlation with  $P_{\max}\text{-C}$  ( $\rho = 0.76$ ,  $p < 0.05$ ).

In addition to non-linear electron transport,  $\phi_{e:c}/n_{\text{PSII}}$  is also affected by the number of Chl energetically coupled to RCII.  
Without directly measuring Chl:RCII, which requires either an FRRF instrument-specific calibration factor or specialized O<sub>2</sub>  
flash yield instrumentation, it is challenging to isolate the drivers of  $\phi_{e:c}/n_{\text{PSII}}$  variability (Oxborough *et al.*, 2012; Xu *et al.*,  
675 2018). Yet, Chl:RCII is known to be sensitive to iron and light availability (Greene *et al.*, 1992; Murphy *et al.*, 2017). Although  
low light acclimated phytoplankton can increase Chl:C to maximize light absorption (Geider, 1987), we did not note a strong  
correlation between the light-acclimation parameter  $E_K$  and  $V_{\max}$  ( $\rho = -0.21$ ,  $p \gg 0.05$ ), indicating that differences in light  
acclimation state was not a primary driver of electron-carbon ratios in our study area. Iron limitation is also expected to increase  
Chl:RCII, because although iron limitation lowers cellular Chl content, and Chl is more likely to be energetically coupled to  
680 RCII rather than PSI reaction centers (Greene *et al.*, 1992). We thus conclude that Fe-stress likely contributed to variability in  
 $\phi_{e:c}/n_{\text{PSII}}$  by driving increases Chl:RCII in addition to influencing non-linear electron transport rates.

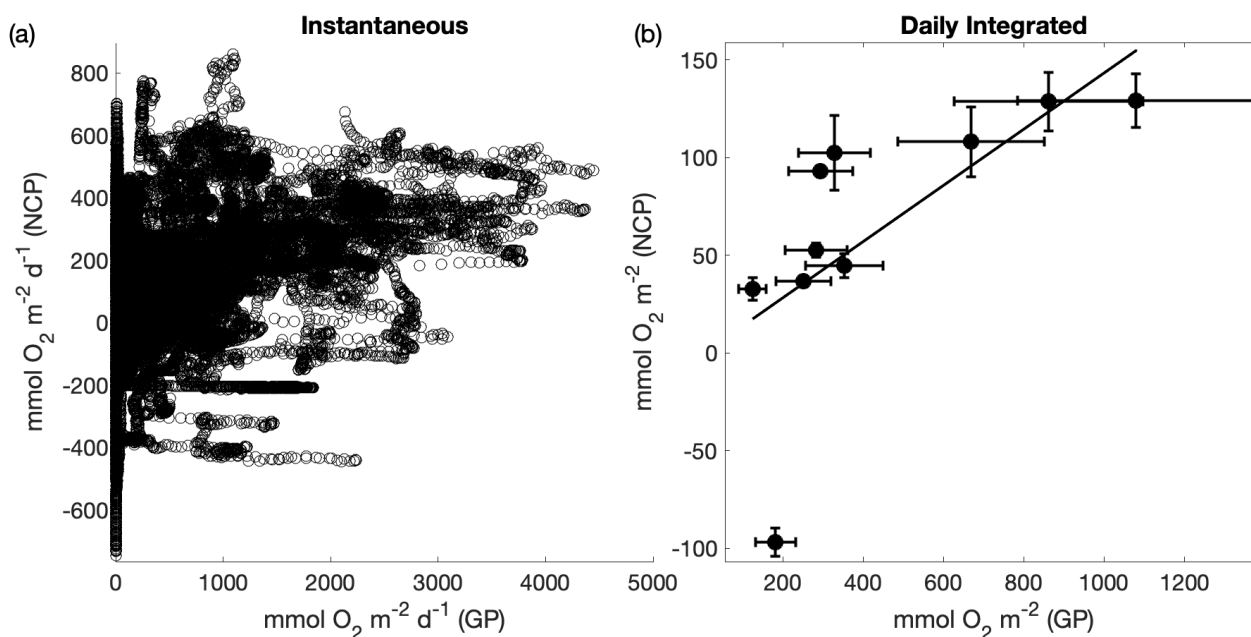
#### 4.3.2 Comparison of $\text{ETR}_{\text{PSII}}$ and NCP

As opposite end members of the productivity spectrum (Fig. 7),  $\text{ETR}_{\text{PSII}}$  quantifies gross photochemical energy production,  
while NCP represents the net accumulation of photosynthetic carbon or oxygen remaining after accounting for all sources of  
685 mixed layer respiration. To directly compare  $\text{ETR}_{\text{PSII}}$  and NCP, we converted  $\text{ETR}_{\text{PSII}}$  from units of  $e^- \text{RCII}^{-1} \text{s}^{-1}$  to  $\text{mmol O}_2$   
 $\text{m}^{-2} \text{d}^{-1}$  (Eq. 5) by assuming each RCII was functionally coupled to 400 – 700 Chl pigments (Kolber and Falkowski, 1993;  
Schuback, Schallenberg, Duckham and Maldonado, 2015) and 4 charge separation events per gross O<sub>2</sub> evolved. The resulting  
O<sub>2</sub>-based gross photochemistry values varied between 0 – 4000  $\text{mmol O}_2 \text{m}^{-2} \text{d}^{-1}$  (Fig. 5c), within range of previously reported  
values for the CCS (Kranz *et al.*, 2020). On average, NCP accounted for  $17 \pm 8\%$  of gross photochemistry, indicating ~80%  
690 of oxygen produced at PSII by water splitting reactions was consumed within the mixed layer through autotrophic and  
heterotrophic respiration. In contrast to  $\phi_{e:c}/n_{\text{PSII}}$ , there was no significant differences in NCP: $\text{ETR}_{\text{PSII}}$  between Cape Blanco,  
Cape Mendocino, or offshore. Although NCP is constrained by gross photochemistry, NCP was greater than  $\text{ETR}_{\text{PSII}}$  over 29%  
of the cruise track. This apparent contradiction can be explained by differences time-scales between instantaneous  $\text{ETR}_{\text{PSII}}$   
measurements, and NCP, which is integrated over O<sub>2</sub> residence times in the mixed layer (~1–2 weeks). Sustained net  
695 autotrophy can lead to accumulation of O<sub>2</sub> in the mixed layer, such that measured O<sub>2</sub> fluxes indicate high levels of NCP despite  
short-term decreases in  $\text{ETR}_{\text{PSII}}$  (e.g. overnight).

Regardless of the large differences in integration time-scales and metabolic sources of decoupling, NCP showed strong  
coherence with  $\text{ETR}_{\text{PSII}}$  (Fig 9). Direct comparison between continuous underway measurements of  $\text{ETR}_{\text{PSII}}$  and NCP yielded  
700 a moderate positive correlation ( $\rho = 0.43$ ,  $p \ll 0.01$ ). To account for some of the decoupling introduced by the strong diel  
dependence of  $\text{ETR}_{\text{PSII}}$ , we also compared  $\text{ETR}_{\text{PSII}}$  and NCP measurements integrated over 24hr bins. This comparison  
indicated a much stronger relationship between  $\text{ETR}_{\text{PSII}}$  and NCP ( $\rho = 0.92$ ,  $p \ll 0.01$ ; Fig 9). Across daily integrated time-  
scales, NCP linearly increased as a function of  $\text{ETR}_{\text{PSII}}$  with a ~15% energy transfer efficiency and a predicted NCP of -0.55



705 mmol O<sub>2</sub> m<sup>-2</sup> when ETR<sub>PSII</sub> is zero. This efficiency estimate is within range of previous studies that have compared gross  
 oxygen production and NCP using triple oxygen isotope and O<sub>2</sub>/Ar methods (Haskell II *et al.*, 2017; Howard *et al.*, 2017),  
 despite the differences in integration time scales between ETR and the triple oxygen isotope method. Further, a sensitivity  
 analysis found no significant changes in the derived energy transfer efficiency between ETR and NCP integrated over 24, 48,  
 72, and 96-hour bins. These results suggest the utility of FRRF to 1) estimate gross oxygen productivity as an alternative to  
 710 triple oxygen isotopes or other discrete methods (e.g. H<sub>2</sub><sup>18</sup>O tracer experiments), and 2) constrain net community productivity  
 estimates.



715 **Figure 9. Comparison between fluorescence-based gross photochemistry (GP) and NCP.** The left subpanel directly  
 compares continuous underway ETR<sub>PSII</sub> and NCP measurements ( $\rho = 0.43$ ,  $p \ll 0.01$ ), while the right panel compares daily-  
 integrated measurements of ETR<sub>PSII</sub> and NCP measurements ( $\rho = 0.92$ ,  $p \ll 0.01$ ). A line of best fit ( $y = 0.14 \cdot GP - 0.55$ ) is  
 drawn through the positive NCP data points. The error bars represent the total uncertainty of each measurement determined  
 by propagating uncertainty in each input variable. For GPP, total uncertainty is dominated by uncertainty in the Chl:RCII,  
 while for NCP, major sources of uncertainty include uncertainty in the deep water supply ratio of O<sub>2</sub>:N<sub>2</sub>O, and modelled  
 720 differences between [N<sub>2</sub>] and [Ar]. Assumption biases (e.g. no horizontal advection of O<sub>2</sub>) also represents a potential large  
 source of uncertainty but was not quantified. A line of best fit is drawn through the positive NCP points on the right plot with  
 the equation  $y = 0.14 \cdot GPP - 0.55$  ( $R^2 = 0.82$ ).

## 5 Conclusion

725 Consistent with previous observations, our results indicate a patchwork of Fe-stress within the coastal upwelling waters of the  
 California Current, providing evidence for physiological Fe-stress within an upwelling filament near Cape Mendocino.  
 Differences in iron availability between upwelling filaments appear to be linked to bathymetric features that influence sediment  
 loading, and variable micronutrient content of sub-surface upwelling source waters. Paired fluorescence- and <sup>14</sup>C-based  
 photosynthesis-irradiance measurements indicated strong connectivity between ETR<sub>PSII</sub> and carbon-fixation in Fe-replete  
 phytoplankton, and greater decoupling in these rates for Fe-limited assemblages, with greater associated variability in  
 730  $\phi_e \cdot C/n_{PSII}$ . Recently, there has been significant focus on understanding  $\phi_e \cdot C/n_{PSII}$  variability to expand FRRF-based GPP  
 surveys (Hughes, Campbell, *et al.*, 2018). Our results suggest that nutrient replete phytoplankton are able maintain near



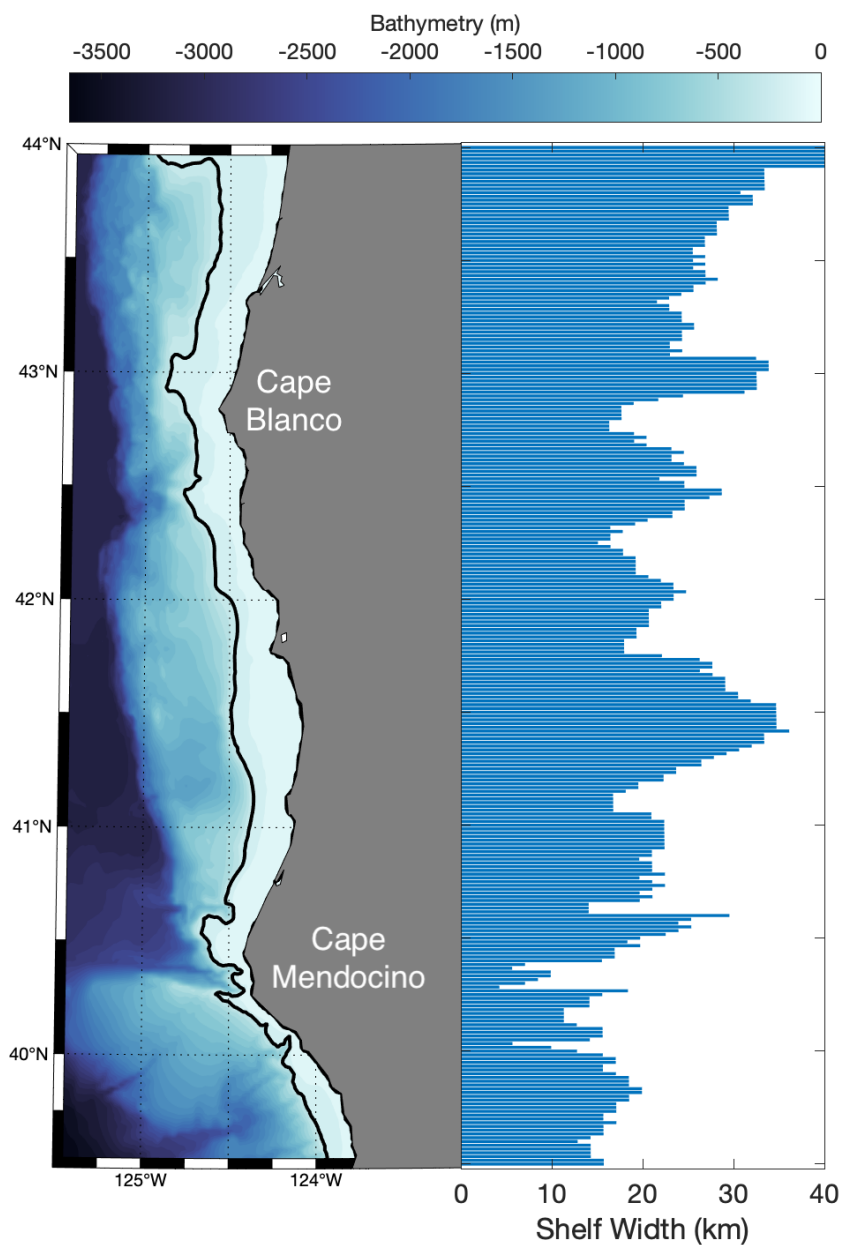


735

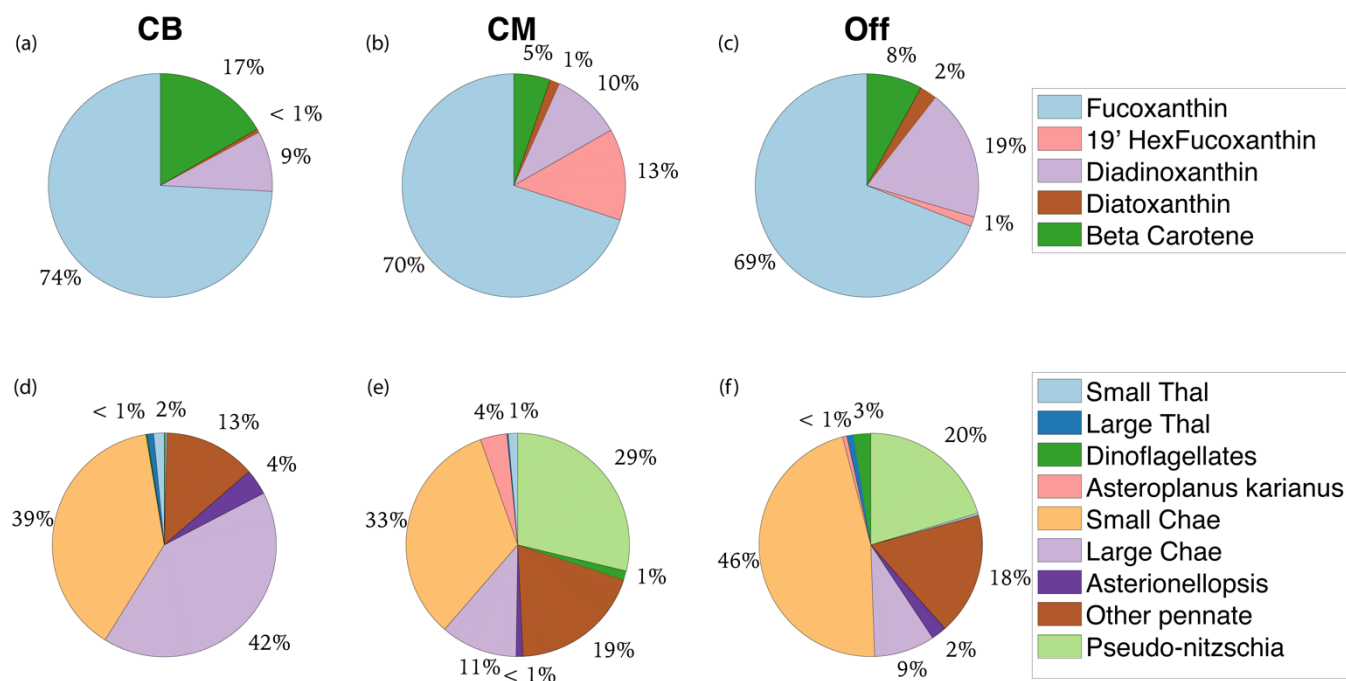
constant  $\phi_e: C/n_{PSII}$  under increasing excitation pressures due to their ability to efficiently transfer energy between PSI and PSII. Under these circumstances,  $NPQ_{NSV}$  is not a good predictor of  $\phi_e: C/n_{PSII}$ . However, where nutrient limitation necessitates enhanced non-linear electron transport pathways to maintain energy balance between PSII and PSI,  $\phi_e: C/n_{PSII}$  does scale with  $NPQ_{NSV}$  and excess excitation pressure. With the accumulation of further data across a range of oceanographic conditions, it may be possible to derive more robust empirical relationships between  $NPQ_{NSV}$  and  $\phi_e: C/n_{PSII}$ , which could be used to derive GPP in C-based units from FRRF measurements. In addition, our results show a strong general coherence between daily integrated  $ETR_{PSII}$  and NCP measurements, suggesting that  $ETR_{PSII}$  may have significant utility as an indicator of bulk primary productivity. We thus conclude that high-resolution, ship-board measurements hold significant potential to explore fine-scale variability in surface water primary productivity in complex coastal waters.



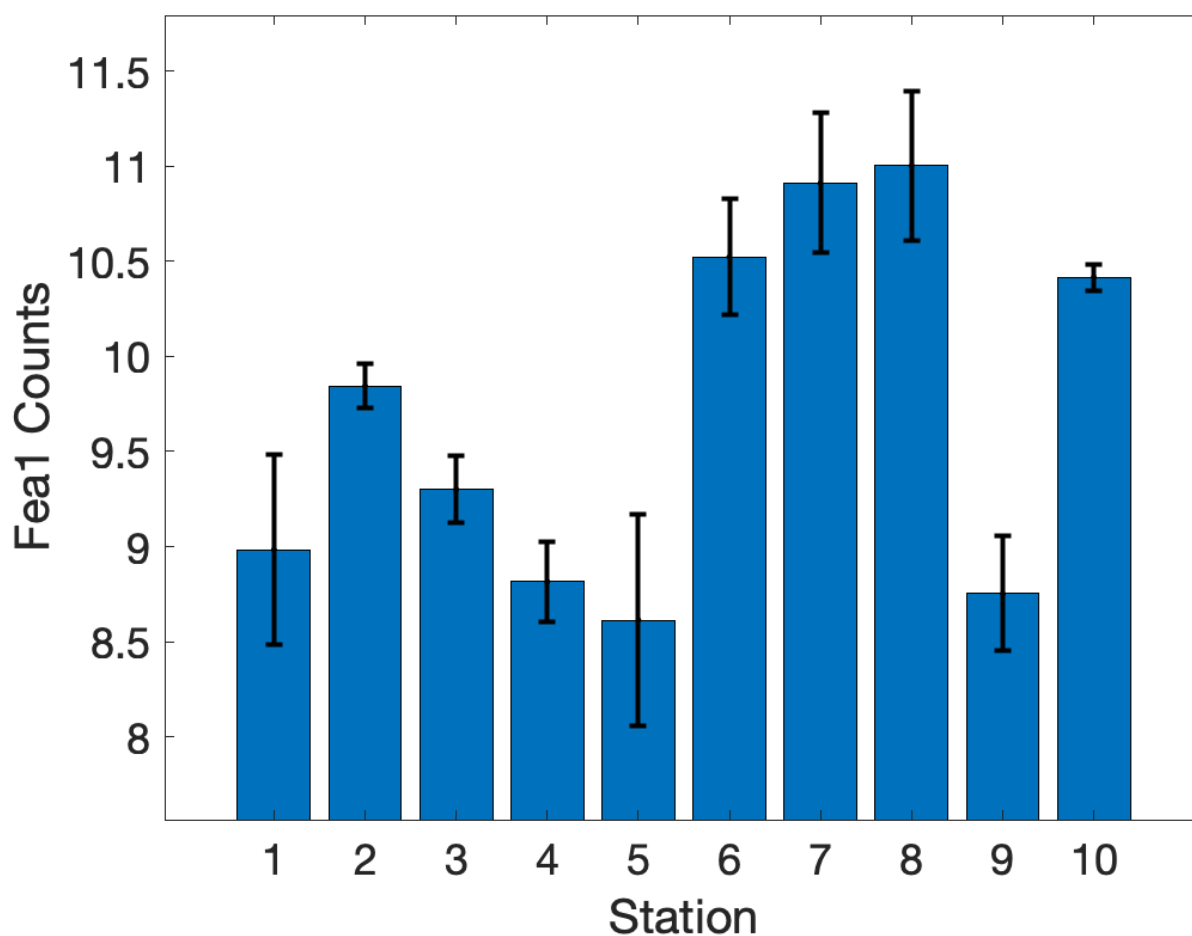
740 6 Appendix



**Appendix 1. Bathymetric map of the study region.** The black contour line indicates the 200m isobath. The horizontal bar graph demonstrates the shelf width at the aligned latitude.



**Appendix 2. Pigment and taxonomic composition of study area sub-regions.** a-c) display non-Chl pigment distribution by mass for Cape Blanco (CB), Cape Mendocino (CM), and Offshore (Off). d-f) display the taxonomic distribution of diatom and dinoflagellate groups visible for microscope counts.



**Appendix 3. Diatom-specific expression of Fe assimilation gene *Fea1*.** Bar height displays *Fea1* count means by station. Error bars display the standard deviation. Stations 1-4 were in close proximity of Cape Blanco, 6 and 10 were offshore while the remaining stations were in proximity of the Cape Mendocino upwelling filament.

## 755 7 Code and data availability

In-situ hydrographic, dissolved gas concentration, and phytoplankton photophysiology data collected during the PUPCYCLE II expedition have been submitted to PANGAEA, an Earth Science data repository, and are being tracked with the submission codes PDI – 39901, 39902, and 39930, respectively. Dissolved Fe data have been submitted to <https://www.bco-dmo.org/>. DOI names are expected to be issued shortly. Satellite SST (11  $\mu$  daytime) and Chl data used to produce Fig 1 were downloaded from NASA Aqua MODIS platform (<https://oceancolor.gsfc.nasa.gov/13/>). Ancillary data required to derive  $N_2'$  were sourced from several public databases. Wind speed and Ekman transport were taken from NOAA's Windspeed, Stress, Curl, Divergence, and Ekman Upwelling, Metop-C ASCAT, 0.25 degree, Global, Near Real Time, 2020-present, 1-Day Composite product. Sea level pressure was downloaded from the US Navy Global Environmental Model (NAVGEM) 0.5 degree, 2013-present Pressure MSL



765 (<https://coastwatch.pfeg.noaa.gov/erddap/griddap/erdNavgem05DPres.html>). Modeled sea surface temperature and salinity products were downloaded from <https://psl.noaa.gov/data/gridded/data.noaa.oisst.v2.highres.html> and [https://podaac.jpl.nasa.gov/dataset/SMAP\\_JPL\\_L3\\_SSS\\_CAP\\_8DAY-RUNNINGMEAN\\_V5](https://podaac.jpl.nasa.gov/dataset/SMAP_JPL_L3_SSS_CAP_8DAY-RUNNINGMEAN_V5), respectively. Model code used to calculate  $N_2'$  and NCP calculations are available at [https://github.com/rizett/O2N2\\_NCP\\_toolbox](https://github.com/rizett/O2N2_NCP_toolbox).

## 8 Author Contributions

770 Y.S. conceived the research plan, conducted FRRF and  $^{14}C$  measurements, analysed data and wrote the manuscript with significant contribution from all co-authors. K.S. operated the PIGI, conducted all  $N_2O$  measurements, and assisted with NCP computations and analysis. E.S. collected macronutrient and meta-transcriptomic data and assisted with meta-transcriptomic analysis. A.M. facilitated meta-transcriptomic data collection, assisted with meta-transcriptomic analysis, and co-organized the PUPCYCLE II expedition with C.T. Trace metal clean Fe samples were collected by C.T. and processed by R.T. Funding was secured by A.M., C.T., and P.T. Primary advisory support and manuscript editing was done by P.T.

## 9 Competing Interests

The authors declare they have no conflict of interest.

## 10 Acknowledgements

780 We would like to thank the crew and fellow scientists aboard the *R/V Sally Ride* who made this work possible and created a delightful working environment. Special thanks to Sachinandan Pillai who provided HPLC data and mobilization assistance. We thank the Bundy lab at the University of Washington for the loan of their trace metal sampling van. We thank D. Patel from the University of North Carolina for performing microscope counts.

## 11 Financial Support

785 Funding for the PUPCYCLE II cruise was provided to AM from a National Science Foundation grant (OCE1751805). Iron analyses were funded through the Research Corporation for Science Advancement's Cottrell Scholar Award #26844 to C.T. Trace metal sampling was conducted with a shared-use rosette maintained at Skidaway and purchased with NSF Award OCE-2015430.

## 12 References

790 Aardema, H. M. *et al.* (2024) 'On the Variability of Phytoplankton Photophysiology Along a Latitudinal Transect in the North Atlantic Surface Ocean', *Journal of Geophysical Research: Biogeosciences*, 129(9), p. e2023JG007962. doi: <https://doi.org/10.1029/2023JG007962>.

795 Allen, M. *et al.* (2007) 'FEA1, FEA2, and FRE1, encoding two homologous secreted proteins and a candidate ferrireductase, are expressed coordinately with FOX1 and FTR1 in iron-deficient *Chlamydomonas reinhardtii*.', *Eukaryot Cell*. doi: 10.1128/EC.00205-07.

Andrews, S. (2010) 'FastQC: a quality control tool for high throughput sequence data.'

Austin, J. A. and Barth, J. A. (2002) 'Variation in the position of the upwelling front on the Oregon shelf', *Journal of*





- 800 *Geophysical Research: Oceans*, 107(C11), pp. 1–15. doi: <https://doi.org/10.1029/2001JC000858>.
- Balch, W. M. *et al.* (2021) ‘Ocean Optics & Biogeochemistry Protocols for Satellite Ocean Colour Sensor Validation IOCCG Protocol Series Volume 7. 0 , 2021 Aquatic Primary Productivity Field Protocols for Satellite Validation and Model Synthesis ( DRAFT ) Report of a NASA-sponsored ’, 7.
- 805 Banse, K. (2002) ‘SHOULD WE CONTINUE TO MEASURE 14C-UPTAKE BY PHYTOPLANKTON FOR ANOTHER 50 YEARS?’, *Limnology and Oceanography Bulletin*, 11(3), pp. 45–46. doi: <https://doi.org/10.1002/lob.200211345>.
- Behnke, J. and LaRoche, J. (2020) ‘Iron uptake proteins in algae and the role of Iron Starvation-Induced Proteins (ISIPs)’, *European Journal of Phycology*. Taylor & Francis, 55(3), pp. 339–360. doi: 10.1080/09670262.2020.1744039.
- 810 Behrenfeld, M. J. *et al.* (2005) ‘Carbon-based ocean productivity and phytoplankton physiology from space’, *Global Biogeochemical Cycles*, 19(1), pp. 1–14. doi: 10.1029/2004GB002299.
- Behrenfeld, M. J. and Falkowski, P. G. (1997) ‘Photosynthetic rates derived from satellite-based chlorophyll concentration’, 815 *Limnology and Oceanography*, 41(January), pp. 1–20. Available at: <https://www.google.com/search?q=Engle+et+al.%2C2000&oq=Engle+et+al.%2C2000&aqs=chrome..69i57.11777j0j8&sourceid=chrome&ie=UTF-8>.
- Behrenfeld, M. J. and Milligan, A. J. (2013) ‘Photophysiological expressions of iron stress in phytoplankton’, 820 *Annual Review of Marine Science*, 5, pp. 217–246. doi: 10.1146/annurev-marine-121211-172356.
- Biller, D. V *et al.* (2013) ‘Coastal iron and nitrate distributions during the spring and summer upwelling season in the central California Current upwelling regime’, *Continental Shelf Research*, 66, pp. 58–72. doi: <https://doi.org/10.1016/j.csr.2013.07.003>.
- 825 Bograd, S. J. *et al.* (2023) ‘Climate Change Impacts on Eastern Boundary Upwelling Systems’, *Annual Review of Marine Science*, 15, pp. 303–328. doi: 10.1146/annurev-marine-032122-021945.
- Bruland, K. W. *et al.* (2005) ‘Iron, macronutrients and diatom blooms in the Peru upwelling regime: brown and blue waters of 830 Peru’, *Marine Chemistry*, 93(2), pp. 81–103. doi: <https://doi.org/10.1016/j.marchem.2004.06.011>.
- Bruland, K. W., Middag, R. and Lohan, M. C. (2014) ‘8.2 - Controls of Trace Metals in Seawater’, in Holland, H. D. and Turekian, K. K. (eds) *Treatise on Geochemistry (Second Edition)*. Second Edi. Oxford: Elsevier, pp. 19–51. doi: <https://doi.org/10.1016/B978-0-08-095975-7.00602-1>.
- 835 Buchfink, B., Xie, C. and Huson, D. H. (2015) ‘Fast and sensitive protein alignment using DIAMOND’, *Nature Methods*, 12(1), pp. 59–60. doi: 10.1038/nmeth.3176.
- Burda, K. *et al.* (2003) ‘Mössbauer studies of the non-heme iron and cytochrome b 559 in a *Chlamydomonas reinhardtii* PSI-mutant and their interactions with  $\alpha$ -tocopherol quinone’, *FEBS Letters*, 535(1–3), pp. 159–165. doi: [https://doi.org/10.1016/S0014-5793\(02\)03895-4](https://doi.org/10.1016/S0014-5793(02)03895-4).
- 840 Bushmanova, E. *et al.* (2019) ‘RnaSPAdes: A de novo transcriptome assembler and its application to RNA-Seq data’, *GigaScience*. Oxford University Press, 8(9), pp. 1–13. doi: 10.1093/gigascience/giz100.
- 845 Carvalho, F. *et al.* (2020) ‘FIRE glider: Mapping in situ chlorophyll variable fluorescence with autonomous underwater gliders’, *Limnology and Oceanography: Methods*, 18(9), pp. 531–545. doi: 10.1002/lom3.10380.



- 850 Cassar, N. *et al.* (2009) ‘Continuous high-frequency dissolved O<sub>2</sub>/Ar Measurements by Equilibrator Inlet Mass Spectrometry’, *Analytical Chemistry*, 81(5), pp. 1855–1864. doi: 10.1021/ac802300u.
- 855 Cassar, N., Nevison, C. D. and Manizza, M. (2014) ‘Correcting oceanic O<sub>2</sub>/Ar-net community production estimates for vertical mixing using N<sub>2</sub>O observations’, *Geophysical Research Letters*, 41(24), pp. 8961–8970. doi: <https://doi.org/10.1002/2014GL062040>.
- Castelao, R. M. and Luo, H. (2018) ‘Upwelling jet separation in the California Current System’, *Scientific Reports*. Springer US, 8(1), pp. 1–8. doi: 10.1038/s41598-018-34401-y.
- 860 Choi, B., Rempala, G. and Kim, J. (2017) ‘Beyond the Michaelis-Menten equation: Accurate and efficient estimation of enzyme kinetic parameters.’, *Sci Rep*. doi: 10.1038/s41598-017-17072-z.
- Craig, H. and Hayward, T. (1987) ‘Oxygen Supersaturation in the Ocean: Biological Versus Physical Contributions’, *Science*, 235(4785), pp. 199–202. doi: 10.1126/science.235.4785.199.
- 865 Cutter, G. *et al.* (2014) ‘Sampling and sample-handling protocols for GEOTRACES cruises. GEOTRACES cookbook’, (December), pp. 1–238. Available at: [http://www.geotraces.org/images/stories/documents/intercalibration/Cookbook\\_v2.pdf](http://www.geotraces.org/images/stories/documents/intercalibration/Cookbook_v2.pdf).  
Deutsch, C. *et al.* (2021) ‘Biogeochemical variability in the California Current System’, *Progress in Oceanography*, 196, p. 102565. doi: <https://doi.org/10.1016/j.pocean.2021.102565>.
- 870 Domingues, R. B. and Barbosa, A. B. (2023) ‘Evaluating Underwater Light Availability for Phytoplankton: Mean Light Intensity in the Mixed Layer versus Attenuation Coefficient’, *Water*, 15(16). doi: 10.3390/w15162966.
- Elkins, J. W. *et al.* (1978) ‘Aquatic sources and sinks for nitrous oxide’, *Nature*, 275(5681), pp. 602–606. doi: 10.1038/275602a0.
- 875 Federhen, S. (2012) ‘The NCBI Taxonomy database’, *Nucleic Acids Research*, 40(D1), pp. D136–D143. doi: 10.1093/nar/gkr1178.
- 880 Fei, S. *et al.* (2024) ‘The linkage between phytoplankton productivity and photosynthetic electron transport in the summer from the Changjiang River to the East China Sea’, *Frontiers in Marine Science*, 11. doi: 10.3389/fmars.2024.1383988.
- 885 GEIDER, R. J. (1987) ‘LIGHT AND TEMPERATURE DEPENDENCE OF THE CARBON TO CHLOROPHYLL a RATIO IN MICROALGAE AND CYANOBACTERIA: IMPLICATIONS FOR PHYSIOLOGY AND GROWTH OF PHYTOPLANKTON’, *New Phytologist*, 106(1), pp. 1–34. doi: <https://doi.org/10.1111/j.1469-8137.1987.tb04788.x>.
- Greene, R. M. *et al.* (1992) ‘Iron-Induced Changes in Light Harvesting and Photochemical Energy Conversion Processes in Eukaryotic Marine Algae 1’, *Plant Physiology*, 100(2), pp. 565–575. doi: 10.1104/pp.100.2.565.
- 890 Groussman, R. D. *et al.* (2023) ‘MarFERReT, an open-source, version-controlled reference library of marine microbial eukaryote functional genes’, *Scientific Data*, 10(1), p. 926. doi: 10.1038/s41597-023-02842-4.
- 895 Grundle, D. S., Juniper, S. K. and Giesbrecht, K. E. (2013) ‘Euphotic zone nitrification in the NE subarctic Pacific: Implications for measurements of new production’, *Marine Chemistry*, 155, pp. 113–123. doi: <https://doi.org/10.1016/j.marchem.2013.06.004>.
- Halsey, K. H. and Jones, B. M. (2015) ‘Phytoplankton Strategies for Photosynthetic Energy Allocation’, *Annual Review of Marine Science*. Annual Reviews, 7(Volume 7, 2015), pp. 265–297. doi: <https://doi.org/10.1146/annurev-marine-010814-015813>.



- 900 Haskell II, W. Z. *et al.* (2017) ‘Annual cyclicality in export efficiency in the inner Southern California Bight’, *Global Biogeochemical Cycles*, 31(2), pp. 357–376. doi: <https://doi.org/10.1002/2016GB005561>.
- Horrihan, S. G., Carlucci, A. F. and Williams, P. M. (1981) ‘Light inhibition of nitrification in sea-surface films’, *Journal of Marine Research*, 39. Available at: [https://elischolar.library.yale.edu/journal\\_of\\_marine\\_research/1559](https://elischolar.library.yale.edu/journal_of_marine_research/1559).
- 905 Howard, E. M. *et al.* (2017) ‘Biological production, export efficiency, and phytoplankton communities across 8000 km of the South Atlantic’, *Global Biogeochemical Cycles*, 31(7), pp. 1066–1088. doi: <https://doi.org/10.1002/2016GB005488>.
- Hughes, D. J., Varkey, D., *et al.* (2018) ‘Impact of nitrogen availability upon the electron requirement for carbon fixation in Australian coastal phytoplankton communities’, *Limnology and Oceanography*, 63(5), pp. 1891–1910. doi: [10.1002/lno.10814](https://doi.org/10.1002/lno.10814).
- Hughes, D. J., Campbell, D. A., *et al.* (2018) ‘Roadmaps and Detours: Active Chlorophyll- a Assessments of Primary Productivity Across Marine and Freshwater Systems’, *Environmental Science and Technology*, 52(21), pp. 12039–12054. doi: [10.1021/acs.est.8b03488](https://doi.org/10.1021/acs.est.8b03488).
- 915 Hughes, D. J. *et al.* (2021) ‘Taxonomic Variability in the Electron Requirement for Carbon Fixation Across Marine Phytoplankton’, *Journal of Phycology*, 57(1), pp. 111–127. doi: <https://doi.org/10.1111/jpy.13068>.
- 920 Hutchins, D. A. *et al.* (1998) ‘An iron limitation mosaic in the California upwelling regime’, *Limnology and Oceanography*, 43(6), pp. 1037–1054. doi: <https://doi.org/10.4319/lno.1998.43.6.1037>.
- Izett, R. W. *et al.* (2018) ‘Refined Estimates of Net Community Production in the Subarctic Northeast Pacific Derived From  $\Delta O_2/Ar$  Measurements With  $N_2O$ -Based Corrections for Vertical Mixing’, *Global Biogeochemical Cycles*, 32(3), pp. 326–350. doi: <https://doi.org/10.1002/2017GB005792>.
- 925 Izett, R. W. (2021) ‘Improved Estimates of Net Community Production in the Subarctic Pacific and Canadian Arctic Ocean Using Ship-Based Autonomous Measurements and Computational Approaches’, (June).
- 930 Izett, R. W. *et al.* (2021) ‘ $\Delta O_2/N_2$ ’ as a New Tracer of Marine Net Community Production: Application and Evaluation in the Subarctic Northeast Pacific and Canadian Arctic Ocean’, *Frontiers in Marine Science*, 8(August), pp. 1–19. doi: [10.3389/fmars.2021.718625](https://doi.org/10.3389/fmars.2021.718625).
- Izett, R. W. and Tortell, P. D. (2020) ‘The pressure of in situ gases instrument (Pigi) for autonomous shipboard measurement of dissolved  $O_2$  and  $N_2$  in surface ocean waters’, *Oceanography*, 33(2), pp. 156–162. doi: [10.5670/oceanog.2020.214](https://doi.org/10.5670/oceanog.2020.214).
- 935 Izett, R. W. and Tortell, P. D. (2021) ‘ $\Delta O/N$ ’ as a tracer of mixed layer net community production: Theoretical considerations and proof-of-concept’, *Limnology and Oceanography: Methods*, 19(8), pp. 497–509. doi: <https://doi.org/10.1002/lom3.10440>.
- 940 Jacox, M. G. *et al.* (2018) ‘Coastal Upwelling Revisited: Ekman, Bakun, and Improved Upwelling Indices for the U.S. West Coast’, *Journal of Geophysical Research: Oceans*, 123(10), pp. 7332–7350. doi: <https://doi.org/10.1029/2018JC014187>.
- King, A. L. and Barbeau, K. A. (2011) ‘Dissolved iron and macronutrient distributions in the southern California Current System’, *Journal of Geophysical Research: Oceans*, 116(C3). doi: <https://doi.org/10.1029/2010JC006324>.
- 945 Knap, A. *et al.* (1996) ‘Protocols for the Joint Global Ocean Flux Study (JGFOS) Core Measurements’, *JGFOS Reoprt Nr. 19*, vi+170 pp, (Reprint of IOC Manuals and Guides 29, UNESCO 1994), p. 198.



- 950 Kolber, Z. and Falkowski, P. G. (1993) 'Use of active fluorescence to estimate phytoplankton photosynthesis in situ', *Limnology and Oceanography*, 38(8), pp. 1646–1665. doi: 10.4319/lo.1993.38.8.1646.
- 955 Kolber, Z. S., Prášil, O. and Falkowski, P. G. (1998) 'Measurements of variable chlorophyll fluorescence using fast repetition rate techniques: Defining methodology and experimental protocols', *Biochimica et Biophysica Acta - Bioenergetics*, 1367(1–3), pp. 88–106. doi: 10.1016/S0005-2728(98)00135-2.
- Kranz, S. A. *et al.* (2020) 'Lagrangian Studies of Marine Production: A Multimethod Assessment of Productivity Relationships in the California Current Ecosystem Upwelling Region', *Journal of Geophysical Research: Oceans*, 125(6), p. e2019JC015984. doi: <https://doi.org/10.1029/2019JC015984>.
- 960 Lampe, R. H. *et al.* (2018) 'Different iron storage strategies among bloom-forming diatoms.', *Proceedings of the National Academy of Sciences of the United States of America*. United States, 115(52), pp. E12275–E12284. doi: 10.1073/pnas.1805243115.
- 965 Li, W. and Godzik, A. (2006) 'Cd-hit: a fast program for clustering and comparing large sets of protein or nucleotide sequences', *Bioinformatics*, 22(13), pp. 1658–1659. doi: 10.1093/bioinformatics/btl1158.
- Li, Z. *et al.* (2021) 'Dynamic Photophysiological Stress Response of a Model Diatom to Ten Environmental Stresses', *Journal of Phycology*, 57(2), pp. 484–495. doi: <https://doi.org/10.1111/jpy.13072>.
- 970 Lohan, M. C., Aguilar-Islas, A. M. and Bruland, K. W. (2006) 'Direct determination of iron in acidified (pH 1.7) seawater samples by flow injection analysis with catalytic spectrophotometric detection: Application and intercomparison', *Limnology and Oceanography: Methods*, 4(6), pp. 164–171. doi: <https://doi.org/10.4319/lom.2006.4.164>.
- 975 Love, M. I., Huber, W. and Anders, S. (2014) 'Moderated estimation of fold change and dispersion for RNA-seq data with DESeq2', *Genome Biology*, 15(12), p. 550. doi: 10.1186/s13059-014-0550-8.
- Lund, J. W. G., Kipling, C. and Le Cren, E. D. (1958) 'The inverted microscope method of estimating algal numbers and the statistical basis of estimations by counting', *Hydrobiologia*, 11(2), pp. 143–170. doi: 10.1007/BF00007865.
- 980 M. Franck, V. *et al.* (2000) 'Iron and silicic acid concentrations regulate Si uptake north and south of the Polar Frontal Zone in the Pacific Sector of the Southern Ocean', *Deep Sea Research Part II: Topical Studies in Oceanography*, 47(15), pp. 3315–3338. doi: [https://doi.org/10.1016/S0967-0645\(00\)00070-9](https://doi.org/10.1016/S0967-0645(00)00070-9).
- 985 Marchetti, A. *et al.* (2017) 'Development of a molecular-based index for assessing iron status in bloom-forming pennate diatoms', *Journal of Phycology*, 53(4), pp. 820–832. doi: <https://doi.org/10.1111/jpy.12539>.
- Marshak, A. R. and Link, J. S. (2021) 'Primary production ultimately limits fisheries economic performance', *Scientific Reports*, 11(1), p. 12154. doi: 10.1038/s41598-021-91599-0.
- 990 Martin, M. (2011) 'Cutadapt removes adapter sequences from high-throughput sequencing reads', *EMBnet.journal [Online]*, (17.1), pp. 10–12. doi: <https://doi.org/10.14806/ej.17.1.200>.
- 995 Mathis, M. *et al.* (2024) 'Enhanced CO<sub>2</sub> uptake of the coastal ocean is dominated by biological carbon fixation', *Nature Climate Change*. Springer US, 14(4), pp. 373–379. doi: 10.1038/s41558-024-01956-w.
- McKew, B. A. *et al.* (2013) 'The trade-off between the light-harvesting and photoprotective functions of fucoxanthin-chlorophyll proteins dominates light acclimation in *Emiliania huxleyi* (clone CCMP 1516)', *New Phytologist*, 200(1), pp. 74–85. doi: <https://doi.org/10.1111/nph.12373>.



- 1000 Menard, H. W. and Dietz, R. S. (1952) ‘Mendocino Submarine Escarpment’, *The Journal of Geology*, 60(3), pp. 266–278. doi: 10.1086/625962.
- Mistry, J. *et al.* (2021) ‘Pfam: The protein families database in 2021’, *Nucleic Acids Research*, 49(D1), pp. D412–D419. doi: 10.1093/nar/gkaa913.
- 1005 Müller, P., Li, X. P. and Niyogi, K. K. (2001) ‘Non-photochemical quenching. A response to excess light energy’, *Plant Physiology*, 125(4), pp. 1558–1566. doi: 10.1104/pp.125.4.1558.
- Murphy, C. D. *et al.* (2017) ‘Quantitating active photosystem II reaction center content from fluorescence induction transients’, *Limnology and Oceanography: Methods*, 15(1), pp. 54–69. doi: 10.1002/lom3.10142.
- 1010 Niebergall, A. K. *et al.* (2023) ‘Evaluation of new and net community production estimates by multiple ship-based and autonomous observations in the Northeast Pacific Ocean’, *Elementa: Science of the Anthropocene*, 11(1), p. 107. doi: 10.1525/elementa.2021.00107.
- 1015 Olson, R. J. (1981) ‘Differential photoinhibition of marine nitrifying bacteria: A possible mechanism for the formation of the primary nitrite maximum’, *Journal of Marine Research*, (39). Available at: [https://elischolar.library.yale.edu/journal\\_of\\_marine\\_research/1541](https://elischolar.library.yale.edu/journal_of_marine_research/1541).
- 1020 Oxborough, K. *et al.* (2012) ‘Direct estimation of functional PSII reaction center concentration and PSII electron flux on a volume basis: A new approach to the analysis of Fast Repetition Rate fluorometry (FRRf) data’, *Limnology and Oceanography: Methods*, 10(MARCH), pp. 142–154. doi: 10.4319/lom.2012.10.142.
- Patro, R. *et al.* (2017) ‘Salmon provides fast and bias-aware quantification of transcript expression’, *Nature Methods*, 14(4), pp. 417–419. doi: 10.1038/nmeth.4197.
- 1025 Pauly, D. and Christensen, V. (1995) ‘Primary production required to sustain global fisheries’, *Nature*, 374(6519), pp. 255–257. doi: 10.1038/374255a0.
- 1030 Pinckney, J. L. *et al.* (2001) ‘Application of photopigment biomarkers for quantifying microalgal community composition and in situ growth rates’, *Organic Geochemistry*, 32(4), pp. 585–595. doi: [https://doi.org/10.1016/S0146-6380\(00\)00196-0](https://doi.org/10.1016/S0146-6380(00)00196-0).
- Platt, T., Gallegos, C. L. and Harrison, W. G. (1980) ‘Photoinhibition of photosynthesis in natural assemblages of marine phytoplankton’, in.
- 1035 Raven, J. A., Evans, M. C. W. and Korb, R. E. (1999) ‘The role of trace metals in photosynthetic electron transport in O<sub>2</sub>-evolving organisms’, pp. 111–149.
- Roncel, M. *et al.* (2016) ‘Iron deficiency induces a partial inhibition of the photosynthetic electron transport and a high sensitivity to light in the diatom *Phaeodactylum tricornutum*’, *Frontiers in Plant Science*, 7(AUG2016), pp. 1–14. doi: 10.3389/fpls.2016.01050.
- 1040 Ryan-keogh, T. J. *et al.* (2020) ‘Deriving a Proxy for Iron Limitation From Chlorophyll Fluorescence on Buoyancy Gliders’, 7(May), pp. 1–13. doi: 10.3389/fmars.2020.00275.
- 1045 Saba, V. S. *et al.* (2011) ‘An evaluation of ocean color model estimates of marine primary productivity in coastal and pelagic regions across the globe’, pp. 489–503. doi: 10.5194/bg-8-489-2011.
- Sarthou, G. *et al.* (2005) ‘Growth physiology and fate of diatoms in the ocean: a review’, *Journal of Sea Research*, 53(1), pp.



25–42. doi: <https://doi.org/10.1016/j.seares.2004.01.007>.

1050

Schallenberg, C. *et al.* (2020) ‘Diel quenching of Southern Ocean phytoplankton fluorescence is related to iron limitation’, pp. 793–812.

1055

Schuback, N., Schallenberg, C., Duckham, C. and Maldonado, M. T. (2015) ‘Interacting Effects of Light and Iron Availability on the Coupling of Photosynthetic Electron Transport and CO<sub>2</sub> -Assimilation in Marine Phytoplankton’, *PLoS ONE*, pp. 1–30. doi: [10.1371/journal.pone.0133235](https://doi.org/10.1371/journal.pone.0133235).

1060

Schuback, N. *et al.* (2016) ‘Diurnal variation in the coupling of photosynthetic electron transport and Diurnal variation in the coupling of photosynthetic electron transport and carbon fixation in iron-limited phytoplankton in the NE subarctic Pacific’, (March). doi: [10.5194/bg-13-1019-2016](https://doi.org/10.5194/bg-13-1019-2016).

Schuback, N. *et al.* (2017) ‘Primary productivity and the coupling of photosynthetic electron transport and carbon fixation in the Arctic Ocean’, *Limnology and Oceanography*, 62(3), pp. 898–921. doi: [10.1002/lno.10475](https://doi.org/10.1002/lno.10475).

1065

Schuback, N., Tortell, Philippe D, *et al.* (2021) ‘Single-Turnover Variable Chlorophyll Fluorescence as a Tool for Assessing Phytoplankton Photosynthesis and Primary Productivity: Opportunities, Caveats and Recommendations’, *Frontiers in Marine Science*, 8, p. 895. doi: [10.3389/fmars.2021.690607](https://doi.org/10.3389/fmars.2021.690607).

1070

Schuback, N. and Tortell, P. D. (2019) ‘Diurnal regulation of photosynthetic light absorption, electron transport and carbon fixation in two contrasting oceanic environments’, *Biogeosciences Discussions*, pp. 1–33. doi: [10.5194/bg-2018-524](https://doi.org/10.5194/bg-2018-524).

Schuler, K. H. and Tortell, P. D. (2023) ‘Impacts of vertical mixing and ice-melt on N<sub>2</sub>O and CH<sub>4</sub> concentrations in the Canadian Arctic Ocean’, *Continental Shelf Research*, 269, p. 105124. doi: <https://doi.org/10.1016/j.csr.2023.105124>.

1075

Sezginer, Y. *et al.* (2021) ‘Irradiance and nutrient-dependent effects on photosynthetic electron transport in Arctic phytoplankton: A comparison of two chlorophyll fluorescence-based approaches to derive primary photochemistry’, *PLoS ONE*, 16(12 December), pp. 1–23. doi: [10.1371/journal.pone.0256410](https://doi.org/10.1371/journal.pone.0256410).

1080

Sezginer, Y. *et al.* (2023) ‘Fluorescence-based primary productivity estimates are influenced by non-photochemical quenching dynamics in Arctic phytoplankton’, *Frontiers in Microbiology*, 14. doi: [10.3389/fmicb.2023.1294521](https://doi.org/10.3389/fmicb.2023.1294521).

Smith, J. M. *et al.* (2014) ‘Differential contributions of archaeal ammonia oxidizer ecotypes to nitrification in coastal surface waters’, *The ISME Journal*, 8(8), pp. 1704–1714. doi: [10.1038/ismej.2014.11](https://doi.org/10.1038/ismej.2014.11).

1085

Soneson, C., Love, M. I. and Robinson, M. D. (2016) ‘Differential analyses for RNA-seq: transcript-level estimates improve gene-level inferences [version 2; peer review: 2 approved]’, *F1000Research*, 4(1521). doi: [10.12688/f1000research.7563.2](https://doi.org/10.12688/f1000research.7563.2).

Spigai, J. J. (1971) *Marine geology of the continental margin off southern Oregon*. Oregon State University.

1090

Stanley, R. H. R. *et al.* (2010) ‘Net community production and gross primary production rates in the western equatorial Pacific’, *Global Biogeochemical Cycles*, 24(4). doi: <https://doi.org/10.1029/2009GB003651>.

Suggett D, Moore M, G. R. J. (2010) ‘Estimating Aquatic Productivity from Active Fluorescence Measurements’.

1095

Suggett, D. J., Moore, C. M. and Geider, R. J. (2011) ‘Chlorophyll a fluorescence in Aquatic Sciences: Methods and Applications’, *Developments in Applied Phycology*.

Sunda, W. G. and Huntsman, S. A. (1997) ‘Interrelated influence of iron, light and cell size on marine phytoplankton growth’, *Nature*, 390(6658), pp. 389–392. doi: [10.1038/37093](https://doi.org/10.1038/37093).



- 1100 Suorsa, M. (2015) ‘Cyclic electron flow provides acclimatory plasticity for the photosynthetic machinery under various  
environmental conditions and developmental stages’, *Frontiers in Plant Science*, 6(September), pp. 1–8. doi:  
10.3389/fpls.2015.00800.
- 1105 Till, C. P. *et al.* (2019) ‘The iron limitation mosaic in the California Current System: Factors governing Fe availability in the  
shelf/near-shelf region’, *Limnology and Oceanography*, 64(1), pp. 109–123. doi: <https://doi.org/10.1002/lno.11022>.
- Tortell, P. D., Schuback, N. and Suggestt, D. J. (2023) *Application of Single Turnover Active Chlorophyll Fluorescence for  
Phytoplankton Productivity Measurements*. 2.0. doi: <http://dx.doi.org/10.25607/OBP-1084>.
- 1110 Tyrrell, T. and Law, C. S. (1997) ‘Low nitrate:phosphate ratios in the global ocean’, *Nature*, 387(6635), pp. 793–796. doi:  
10.1038/42915.
- 1115 Wang, S. *et al.* (2020) ‘Lagrangian Studies of Net Community Production: The Effect of Diel and Multiday Nonsteady State  
Factors and Vertical Fluxes on O<sub>2</sub>/Ar in a Dynamic Upwelling Region’, *Journal of Geophysical Research: Biogeosciences*,  
125(6), p. e2019JG005569. doi: <https://doi.org/10.1029/2019JG005569>.
- Xu, K. *et al.* (2018) ‘Phytoplankton  $\sigma$ PSII and excitation dissipation; Implications for estimates of primary productivity’,  
*Frontiers in Marine Science*, 5(AUG). doi: 10.3389/fmars.2018.00281.
- 1120 Zhu, Y. *et al.* (2017) ‘Relationship between light, community composition and the electron requirement for carbon fixation in  
natural phytoplankton’, *Marine Ecology Progress Series*, 580, pp. 83–100. doi: 10.3354/meps12310.